Geant4 Monte Carlo simulation of absorbed dose and radiolysis yields enhancement from a gold nanoparticle under MeV proton irradiation

H. N. Tran[a,b,*], M. Karamitros[c], V. N. Ivanchenko[d], S. Guatelli[e,f], S. McKinnon[e,f], K. Murakami[g], T. Sasaki[g], S. Okada[g], M.C. Bordage[h,i], Z. Francis[j], Z. EL Bitar[k], M. A. Bernal[l], J. I. Shin[m], S. B. Lee[n], Ph. Barberet[o,p], T.T. Tran[q], J. M. C. Brown[r,s], T. V. Nhan Hao[t,u], S. Incerti[a,b,o,p]

[a]Division of Nuclear Physics, Ton Duc Thang University, Tan Phong Ward, District 7, Ho Chi Minh City, Vietnam.

[b]Faculty of Applied Sciences, Ton Duc Thang University, Tan Phong Ward, District 7, Ho Chi Minh City, Vietnam.

[c]Notre Dame Radiation Laboratory, University of Notre-Dame, Indiana 46556, USA.

[d]Geant4 Associate International Ltd, Hebden Bridge, U.K.

[e]Centre For Medical Radiation Physics, University of Wollongong, Australia.

[f] Illawarra Health and Medical Research, University of Wollongong, NSW, Australia.

[g]Computing Research Center, High Energy Accelerator Organization, KEK, Tsukuba City, Japan.

[h]INSERM, UMR 1037, CRCT, F-31000 Toulouse, France.

[i]Univ. Toulouse III-Paul Sabatier, UMR 1037, CRCT, F-31000 Toulouse, France.

[j]Saint Joseph University, Faculty of Sciences, Department of Physics, Beirut, Lebanon.

[k]Institut Pluridisciplinaire Hubert Curien/IN2P3/CNRS, Strasbourg, France.

[l]Instituto de FísicaGlebWataghin, Universidade Estadual de Campinas, SP, Brazil.

[m]Division of Heavy Ion Clinical Research, Korea Institute of Radiological and Medical Science, 75, Nowon-ro, Nowon-gu, Seoul, Korea.

[n]Proton Therapy Center, National Cancer Center, 323, Ilsan-ro, Ilsandong-gu,Goyang-si, Gyeonggi-do, Korea.

[o]Univ. Bordeaux, CENBG, UMR 5797, F-33170 Gradignan, France.

[p]CNRS, IN2P3, CENBG, UMR 5797, F-33170 Gradignan, France.

[q]VNUHCM-University of Science, Vietnam.

[r]School of Physics and Astronomy, Monash Universiy, Melbourne, Australia.

[s]School of Mathematics and Physics, Queen's University Belfast, Belfast, Northern Ireland, U.K.

[t]Center of Research and Development, Duy Tan University, K7/25 Quang Trung, Danang, Vietnam.

[u]Department of Physics, College of Education, Hue University, 34 Le Loi Street, Hue City, Vietnam.

Abstract

Gold nanoparticles have been reported as a possible radio-sensitizer agent in radiation therapy due to their ability to increase energy deposition and subsequent direct damage to cells and DNA within their local vicinity. Moreover, this increase in energy deposition also results in high yields of chemical species which have been previously shown to significantly contribute to cellular damage. In this work we present, for the first time, an in-silico investigation utilising the general purpose Monte Carlo simulation toolkit Geant4 into energy deposition and radical species production around a spherical gold nanoparticle 50 nm in diameter via proton irradiation. Simulation were preformed for incident proton energies ranging from 2 to 170 MeV, which are of interest for clinical proton therapy.

Keywords

Geant4-DNA, Gold nanoparticle, radiolysis, proton beam, radiation therapy, radiotherapy, Monte Carlo simulation, radiation chemistry;

Corresponding author

Hoang Ngoc Tran

Division of Nuclear Physics, Ton Duc Thang University, Tan Phong Ward, District 7, Ho Chi Minh City, Vietnam.

Faculty of Applied Sciences, Ton Duc Thang University, Tan Phong Ward, District 7, Ho Chi Minh City, Vietnam.
Tel: + (84-8) 377 55 053; fax: + (84-8) 377 55 055
E-mail address: tranngochoang@tdt.edu.vn (or) ngochoang.tran.vn@gmail.com

1. Introduction

In order to identify potential new approaches for improving clinical outcomes in radiation therapy, and reduce collateral effects, further study of the use of ionizing radiation in healthcare is needed.

One of the most promising new methods in clinical radiation therapy is the delivery of chemical compounds made of high-Z materials to the site of cancerous cells for which ionizing radiation interaction cross sections are significantly higher than in liquid water, the main compound of biological media. As a result, the absorbed dose from irradiation may be enhanced in tumor tissues. For instance, the use of high-Z materials as radio-sensitizers agents was described by Matsudaira *et al.* in 1980 [1], who measured a radio-enhancing effect of iodine on cultured cells irradiated with X-rays but not with gamma rays. The absorbed dose from low energy photon irradiation (X-rays) was increased due to a larger photoelectric cross section in such materials compared to water. This work was then followed by the studies of refs [2] to [6] which utilised iodine and barium containing contrast agents in diagnostic imaging as radio-sensitizers in order to demonstrate their therapeutic advantage in tumors irradiated with low energy photons.

Due to their small size, gold nanoparticles (GNP) have been found to easily penetrate cells [7]. Exposure of human cells to such nanoparticles (NP) does not cause cytotoxicity [8]. In the initial studies of gold nanoparticles using X-rays, Regulla *et al.* [9] found a factor of 100 of dose enhancement in tissue-equivalent polymethylmethacrate close to the surface of a thin metallic gold foil. In experimental studies on mice, Herold *et al.* [10] and Hainfeld *et al.* [11] have found an increased biologically effective dose thanks to the use of gold nanoparticles in

X-ray therapy. For nearly a decade, one has observed *in vivo* the increase of DNA double-strand breaks in irradiated cell populations loaded with gold nanoparticles [12]. The *in vivo* study of Liu *et al.* [13] demonstrated a ~2-45% decrease of cell survival after irradiation using polyethylene-glycol-Au nanoparticles. Recently, Kim *et al.* [14] underlined the role of secondary electrons and characteristic X-rays emitted from metallic nanoparticles irradiated by protons and observed *in vivo* complete tumor regression increase with dose in mice tumors, as well as *in vitro* intracellular reactive oxygen species level increase with dose.

In order to understand the possible mechanisms involved in the observed radio-sensitizing effect induced by GNPs under ionizing irradiation, various studies based on Monte Carlo simulations have been undertaken. Such simulations have the potential to fully describe interaction processes of ionizing radiation in biological materials [15]. These investigations focus on the estimation, at the nano-scale, of energy deposition in the vicinity of a single GNP [16] [17] [18]. For instance, Lechtman *et al.* [16] compared Monte Carlo simulations at the nano-scale with experimental macroscopic dose enhancement predictions to demonstrate the influence of gold nanoparticle intracellular localization. A good agreement was shown between experimental survival and the Monte Carlo-based AuNP radiosensitization predictive model (ARP), which takes into account the detailed energy deposition at the nano-scale. Based on Monte Carlo simulations using the BEAMnrc/DOSXYZnrc codes and the interaction cross sections of the PEGS4 and EGS4 codes, Cho [19] has shown a dependence of the dose enhancement factor (DEF) with the concentration of GNPs within the tumor. In the approach of Jones *et al.* [20], the Monte Carlo code EGSnrc was used to quantify the dose distribution from secondary electron dose point kernels within a GNP-loaded tumor; they demonstrated that the microscopic dose around a GNP is enhanced by factors up to more than 100. More recently, Lin *et al.* [21] performed a comparison of dose in the vicinity of a single GNP and a water nanoparticle (WNP) for various energies of incident photons and protons in connection to radiotherapy. They predicted a dose enhancement up to 14, independently of the proton energy.

Ionizing particles that pass through biological materials can create reactive oxygen species which can participate in unwanted reactions resulting in cell damage, during the so-called "chemical" and "biological" stages lasting from a few picoseconds to many months after irradiation. This was reported *in vivo* in the experiment of Baluchamy *et al.* [22] which showed that proton irradiation alters oxidant and antioxidant levels in cells.

The description of the physical interactions, such as electronic excitations and ionizations, between the ionizing particles and the medium, as well as the rearrangement of the targeted molecules and the subsequent chemistry, can enable us to estimate numerically the amount and types of the generated radiolytic species. Among these species, two, namely the hydroxyl radical and the solvated electron, are created in a significant amount and are particularly reactive. Karamitros *et al*. [23], in the framework of the Geant4-DNA project [24], reported the development of a mechanistic model of radiation chemistry in Geant4, in particular for the evaluation of the yields of hydroxyl radicals and solvated electrons. The potential of enhancement of reactive species production due to an increase of the relative dose distribution around GNPs in an aqueous environment has been recently mentioned in the work of Kim *et al.* [14]. In view of the findings of Kim *et al.* [14], regarding the enhancement of reactive species production around GNP, and in order to further understand the role of GNP, we used in this work for the first time the Geant4 general purpose Monte Carlo simulation toolkit [25] and its very low energy "Geant4-DNA" extension to simulate absorbed dose distributions and production of chemical species generated in the vicinity of a single GNP irradiated by a proton. These quantities are estimated as a function of the distance from the NP. The results are obtained for incident mono-energetic protons ranging from 2 MeV to 170 MeV impacting the GNP and are compared to the results obtained when the GNP is replaced by liquid water (water nanoparticle, noted as WNP).

Section 2 presents a brief description of the Geant4 simulation toolkit and outlines our implementation with specific emphasis on the selected physics processes. Section 3 then

presents and discusses the results of our simulations focusing on the impact of the GNP in liquid water on the observed absorbed dose (Section 3.1) and radiolysis enhancement (Section 3.2). Finally, an overall conclusion follows in Section 4.

2. Materials and methods

2.1 The simulation toolkit

Geant4 is a general purpose and open source Monte Carlo toolkit allowing the simulation of particle-matter interactions. It is nowadays utilized in a variety of application domains, from high energy physics, to aerospace and medical physics [25] [26]. Users can simulate physical interactions by specifying to Geant4 the list of physics "processes" and "models" for all particles involved in the simulation. A physics "process" describes a physical interaction (such as ionization, multiple scattering…) and can evoke several physics "models" (which can be fully theoretical, semi-empirical…). Such models compute the physical interaction total cross section and fully describe the final state of the colliding system, including the production of secondary particles, energy loss and emission angles.

Geant4 has been recently extended to microdosimetry and nanodosimetry applications in liquid water at very low energies and submicrometer scale [27]-[28] in the framework of the Geant4-DNA project. As a component of Geant4 electromagnetic physics, Geant4-DNA currently simulates the dominant physical interactions of electrons, hydrogen and helium atoms with charge states (H^0, H^+, He^0, He^+, He^{2+}) in liquid water down to very low energies [24], [29]. The physico-chemical and chemical module in Geant4-DNA [30] was released for the first time in Geant4 10.1 (December 2014). This module is intended for the simulation of radiolytic species production, their diffusion, and their mutual interactions in liquid water following the modeling of physical interactions [23]. In this study, we use Geant4-DNA to calculate the energy deposition and the distribution of chemical species in liquid water surrounding the nanoparticles. In parallel, Geant4 electromagnetic physics are used for the simulation of physical interactions in GNP and WNP, as ad-hoc low energy physics models are not currently

available in Geant4-DNA for materials other than liquid water. The list of Geant4 electromagnetic processes and models used in this study is given in Table 1 for protons, electrons and photons. This combination is possible since Geant4-DNA physics and Geant4 electromagnetic physics use the same software design. The "Livermore" set [31] of physics models in Geant4 low energy electromagnetic physics was selected for the simulation of electron interactions in the NP. A step size limit of 1 nm and secondary particle production threshold of 13.6 eV (the first ionization level of H) were selected. Atomic de-excitation was activated in order to simulate fluorescence, Auger electron production and particle induced X-ray emission (PIXE). No production threshold has been applied on atomic de-excitation products. The interactions of secondary photons are described by the "Livermore" set of physics models.

Physical interaction	**Geant4 process class**	**Geant4 model class**	**Energy range**
		Electron	
Multiple Scattering	G4eMultipleScattering	G4UrbanMscModel	< 100 MeV
		G4WentzelVIModel	
Coulomb Scattering	G4eCoulombScattering	G4eCoulombScatteringModel	> 100 MeV
Ionization	G4eIonisation	G4LivermoreIonisationModel	< 0.1 MeV
		G4MollerBhabhaModel	> 0.1 MeV
Bremsstrahlung	G4eBremsstrahlung	G4LivermoreBremsstrahlungModel	
		Proton	
Multiple Scattering	G4hMultipleScattering	G4UrbanMscModel	
Ionization	G4hIonisation	G4BraggModel	< 2 MeV

		G4BetheBlochModel	> 2 MeV
		Photon	
Photoelectric effect	G4PhotonElectricEffect	G4LivermorePhotoElectricModel	
Compton scattering	G4ComptonScattering	G4LivermoreComptonModel	
Rayleigh scattering	G4RayleighScattering	G4LivermoreRayleighModel	
Gamma conversion	G4GammaConversion	G4LivermoreGammaConversionModel	

Table 1: Geant4 physics processes and models used for the simulation of electron, proton and photon interactions in the GNP and WNP. Process and model classes are indicated, as well as the energy range of applicability of each model.

2.2 Irradiation conditions

The simulation geometry was comprised of a single NP immersed in liquid water irradiated with mono-energetic proton beam. We chose a NP with a diameter of 50 nm as suggested by Chithrani *et al.* [12] and Lin *et al.* [21]. The transverse size of the proton beam was limited within a circle of a 50 nm diameter in front of the surface of the NP. The propagation axis of the proton beam was set parallel to the z-axis (see Figure 1) and nine different energies were simulated: 2, 3, 5, 10, 30, 50, 75, 100, and 170 MeV. In order to score energy depositions, we divided the region around the NP in 170 spherical shells of log-scale thickness, from the NP's

surface to 10^7 nm. All energy depositions are recorded in these spherical shells. The incident protons are shot from the surface of the NP as a parallel beam and they are stopped when the protons exit the NP in order to avoid the influence of energy deposition by protons in the scoring shells, as shown in Figure 1.

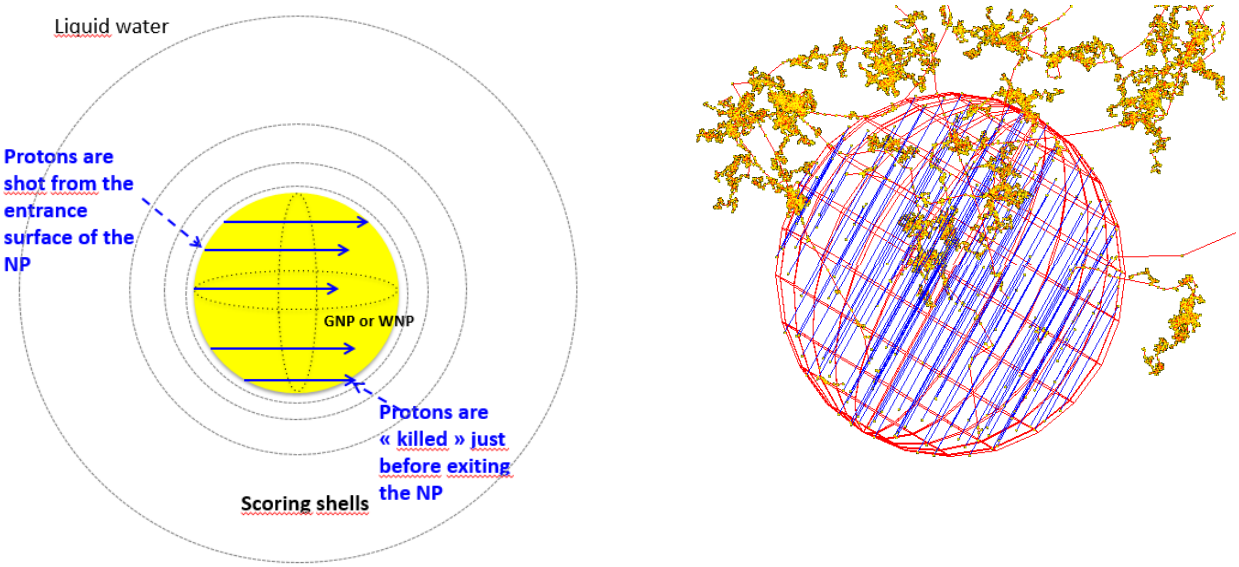

Figure 1: Left: schematic diagram of the simulated geometry showing the incident parallel protons (full line) inside the NP (yellow sphere) and the scoring concentric spherical shells. Right: example of visualization obtained with Geant4 when the NP (in red) is irradiated with a parallel proton beam (blue tracks), showing emitted secondary electron interactions (red tracks and yellow vertices).

2.3 Analysis

The number of selected incident protons were fixed to 10^7 projectiles for GNP and to 10^8 projectiles for WNP to ensure good statistics and reasonable computing times for the radiolysis simulation. Deposited energy was accumulated for all secondary interacting particles. Normalized radial absorbed dose distribution per proton was obtained via the division of the total energy deposited in each spherical shell by the mass of the corresponding shell and number of incident protons. To evaluate the effectiveness of GNP, we estimated the absorbed dose enhancement factor (DEF) by secondary particles outside the NP via the calculation of the

ratio of the dose absorbed outside the GNP with respect to dose absorbed outside the WNP [21]. Only the NP particle material – gold or liquid water – was changed between these two simulations (geometry and physics were not modified).

3. Results and discussion

3.1 Absorbed dose enhancement

Figures 2, 3 and 4 show the comparison of simulated radial absorbed dose distributions in liquid water outside the NP, in the case of a GNP or a WNP, as a function of radial distance from the NP. Results are presented for 2, 3, 5, 10, 30, 50, 75, 100 and 170 MeV incident protons. The energy deposited in liquid water outside the NP is primarily due to the secondary electrons that are generated within and then exit the NP. In all cases, the absorbed dose rapidly decreases as a function of radial distance. In addition, the dose absorbed in liquid water due to secondary electrons emitted from the GNP is always larger than the absorbed dose due to electrons emitted by the WNP, for a given incident proton energy. This is expected as protons interacting with gold will generate significantly more secondary electrons through ionization in the NP than in the water case. Therefore, since the number of secondary electrons are more numerous per interaction and gold is denser than water, the secondary electrons that exit the GNP will deposit more energy outside the NP.

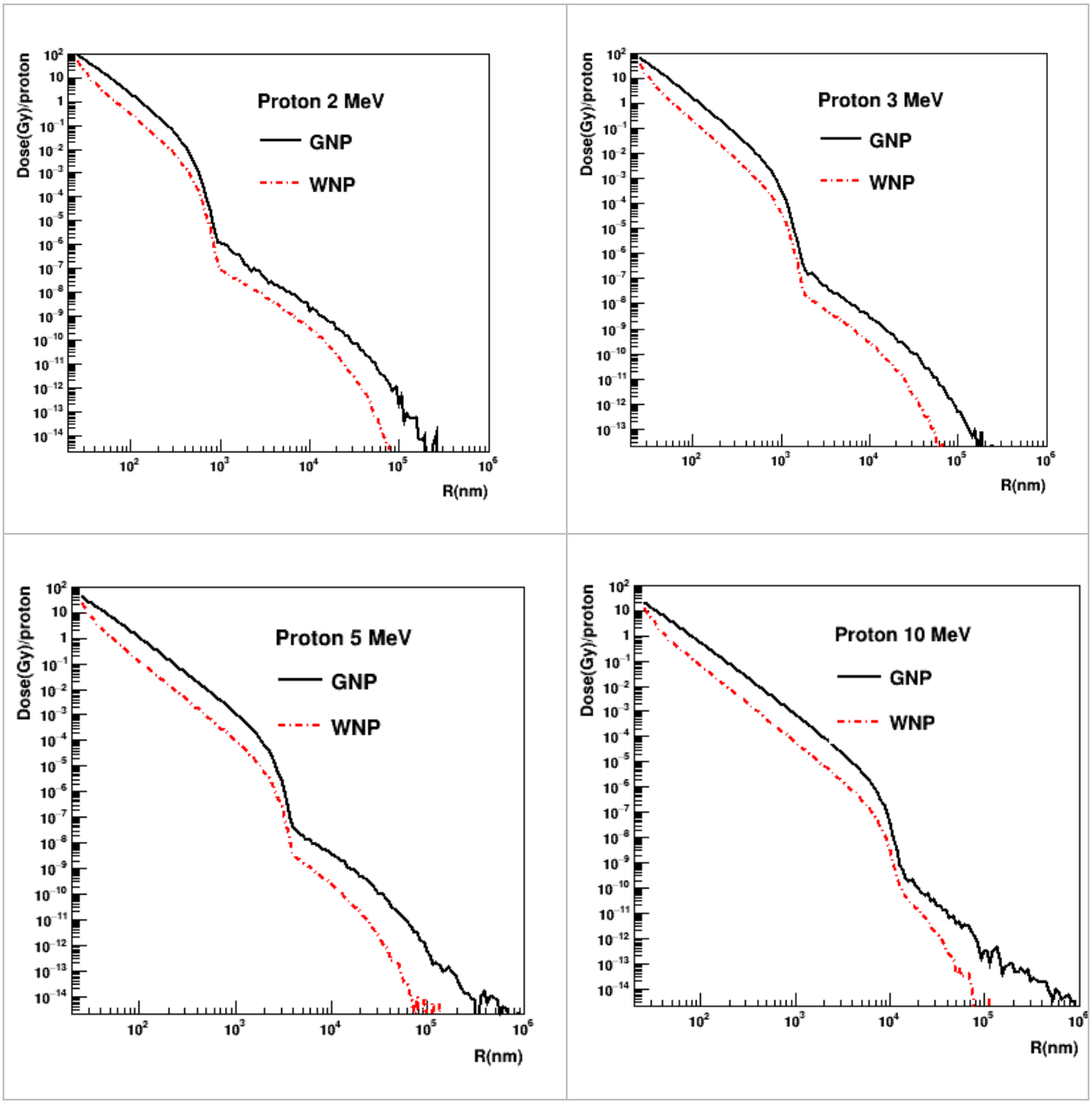

Figure 2: Comparison of radial absorbed dose distribution for GNP (full black lines) and WNP (red dot-dashed lines) for 2 MeV, 3 MeV, 5 MeV and 10 MeV incident protons.

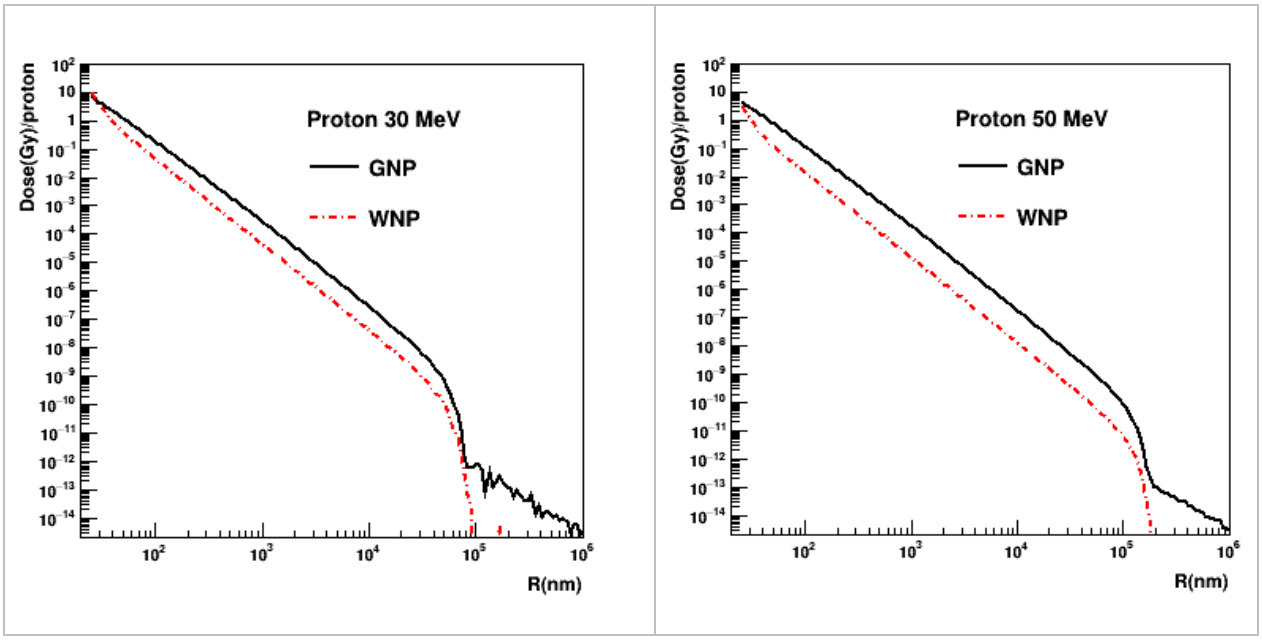

218 *Figure 3: Comparison of radial absorbed dose distribution for GNP (full black lines) and*

219 *WNP (red dot-dashed lines) for 30 MeV and 50 MeV incident protons.*

220

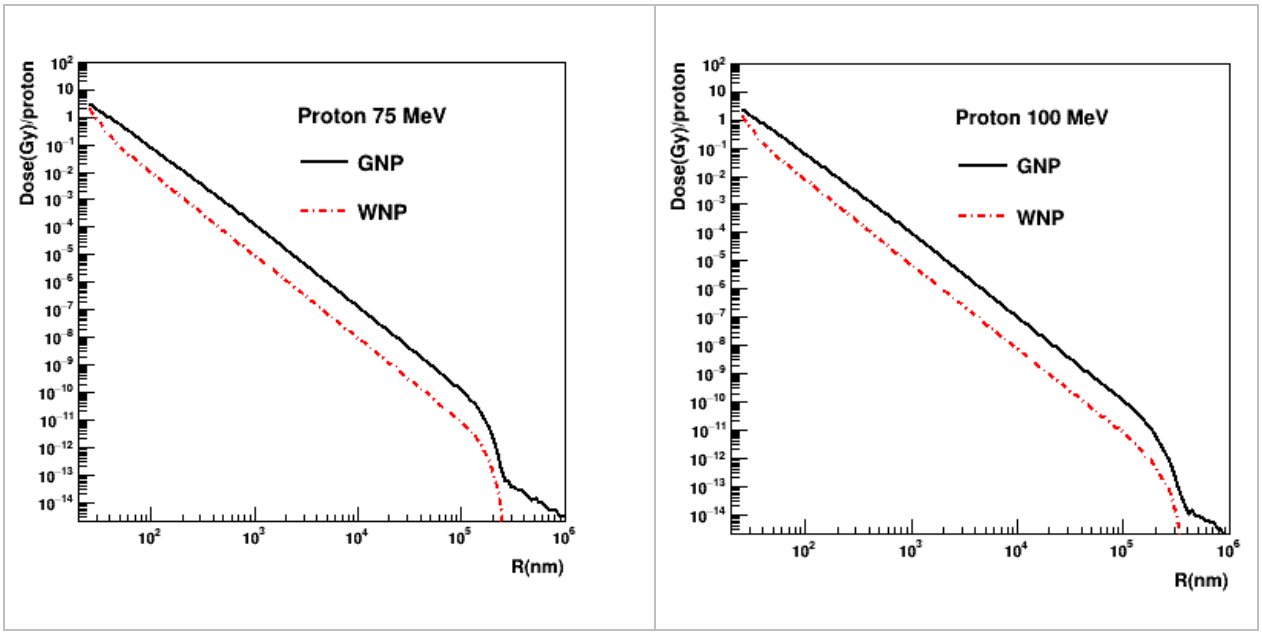

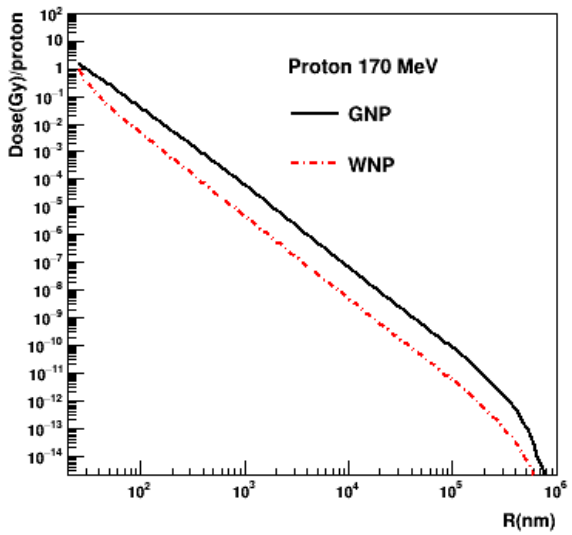

Figure 4: Comparison of radial absorbed dose distribution for GNP (full black lines) and WNP (red dot-dashed lines) for 75 MeV, 100 MeV and 170 MeV incident protons.

The influence of secondary photons on the radial absorbed dose distribution can be observed in the case of 2 MeV incident protons at large distances (r > 1 µm) from the NP surface for both of GNP and WNP (and at larger distances for the three other incident energies as seen in Figure 2). The maximum energy transferred by a 2 MeV proton to a free and at-rest electron is approximately 4.4 keV. This electron has a range in water of about 1 µm, according to our estimations, which is consistent with the results shown in Figure 2.

Thus the observed gradient continuation beyond 1 um in Figure 2 can be attributed to the interaction of secondary photons with the surrounding liquid water medium. These photons are generated through bremsstrahlung and atomic de-excitation in the NP. They can exit the NP and interact by photoelectric effect or Compton scattering in the water medium generating photoelectrons at large distances, which cannot be reached by secondary electrons produced by proton impact. The left panel in Figure 5 shows an example of this effect for 2 MeV incident protons through the comparison of radial absorbed dose surrounding the GNP with (blue points) and without (full black dotted line) the inclusion of energy depositions due to secondary

photons. This figure clearly illustrates the contribution of secondary photons to radial absorbed dose. Further evidence of their contribution can be observed in the radial absorbed dose distributions for electrons and photons at 2 MeV shown in the right panel of Figure 5. Here it can be seen that the contribution from photons to the total absorbed radial dose is negligible in comparison to electrons at distances below 1 um.

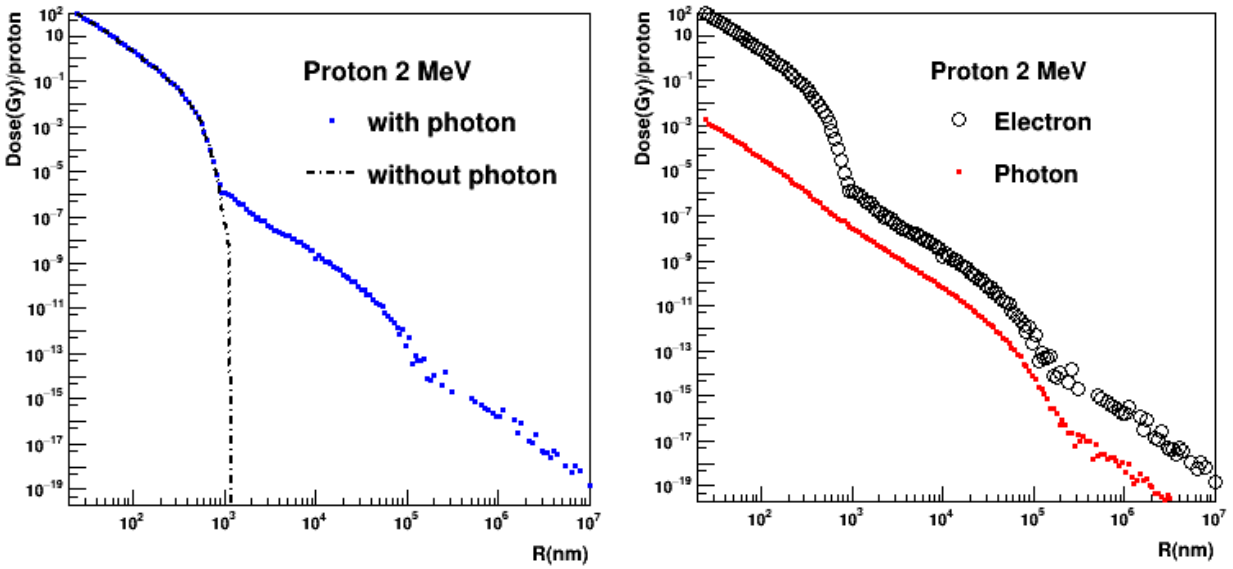

Figure 5: (Left): Comparison of radial absorbed dose distribution around a GNP irradiated by 2 MeV protons, when photoelectron production is deactivated (dot-dash black line) and when it is activated (dot blue line). (Right): Comparison of electron (open circles) and photon (red square) contributions to the radial absorbed dose.

Figure 6 shows the comparison of the energy spectra of secondary photons for the GNP and WNP irradiated by 10^8 protons, for the 2 MeV and 170 MeV cases. For this specific configuration, which does not require the simulation of the chemical stage but only physical interactions, we used identical statistics for GNP and WNP. The number of photons generated by the GNP is larger than the number of photons created by the WNP. In the case of the GNP, the dominant deexcitation lines are observed: $M_{\alpha 1}$ (2 keV), $L_{\alpha 1}$, $L_{\alpha 2}$, $L_{\beta 1}$, $L_{\beta 2}$ and L_{γ} (from 9 keV to 13 keV) for 2 MeV protons. For 170 MeV protons, dominant $K_{\alpha 1}$, $K_{\alpha 2}$ and $K_{\beta 1}$ lines are

observed (68-78 keV, see details on de-excitation lines in [32]). K line of Oxygen at 524 eV is also observed for the WNP. The bremsstrahlung background is also observed in both cases.

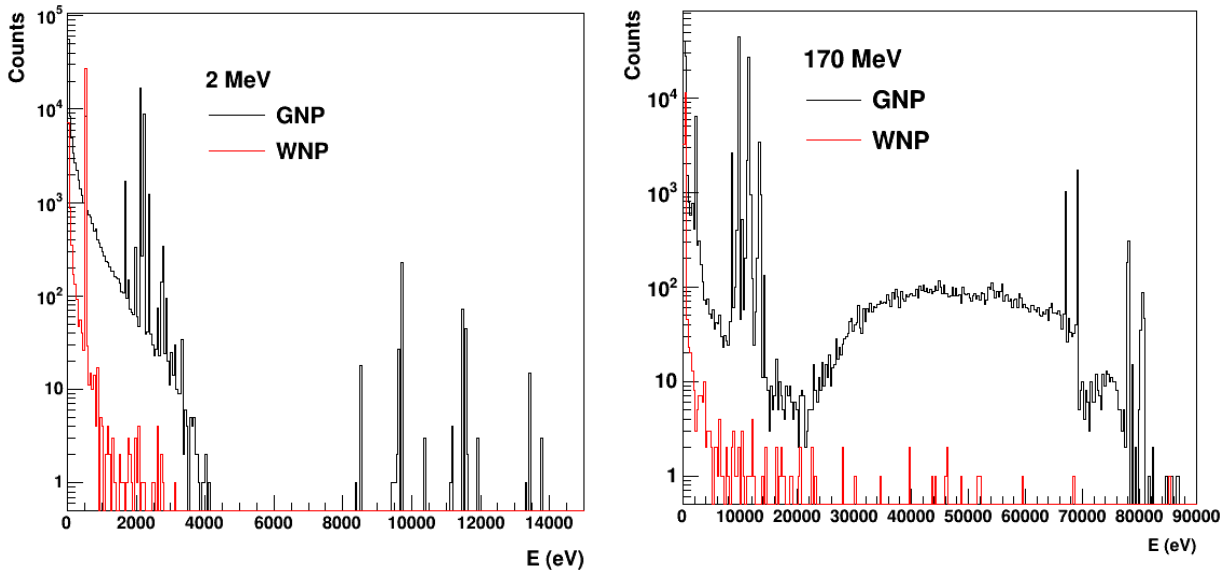

Figure 6: Comparison of the energy spectrum of secondary photons for the GNP (black line) and the WNP (red line) irradiated by 10^8 protons, for the 2 MeV (left) and 170 MeV (right) cases. .

Figure 7 shows the comparison of absorbed dose as a function of radial distance from the GNP for nine incident proton energies (2, 3, 5, 10, 30, 50, 75, 100 and 170 MeV). Up to approximately 1 cm from the GNP all curves have the same monotonic dependence with radial dose; i.e. the larger the kinetic energy of the protons, the smaller the absorbed radial doses. This is also expected since for the selected incident energy range (2 MeV – 170 MeV) the linear energy transfer of protons in the GNP decreases with increasing kinetic energy, leading to a decrease of the production of secondary electrons in the GNP and thus a decreasing absorbed dose in liquid water outside the NP at a given radial distance. The range of secondary electrons produced by the projectile impact increases as the incident proton kinetic energy increases; this is explained by the fact that the maximum energy transferred from a proton to a

free and at-rest electron (as those in valence shells or quasi-free electrons in metals) increases linearly with the proton energy. These electrons determine the gradient-discontinuity region observed in the radial dose curve.

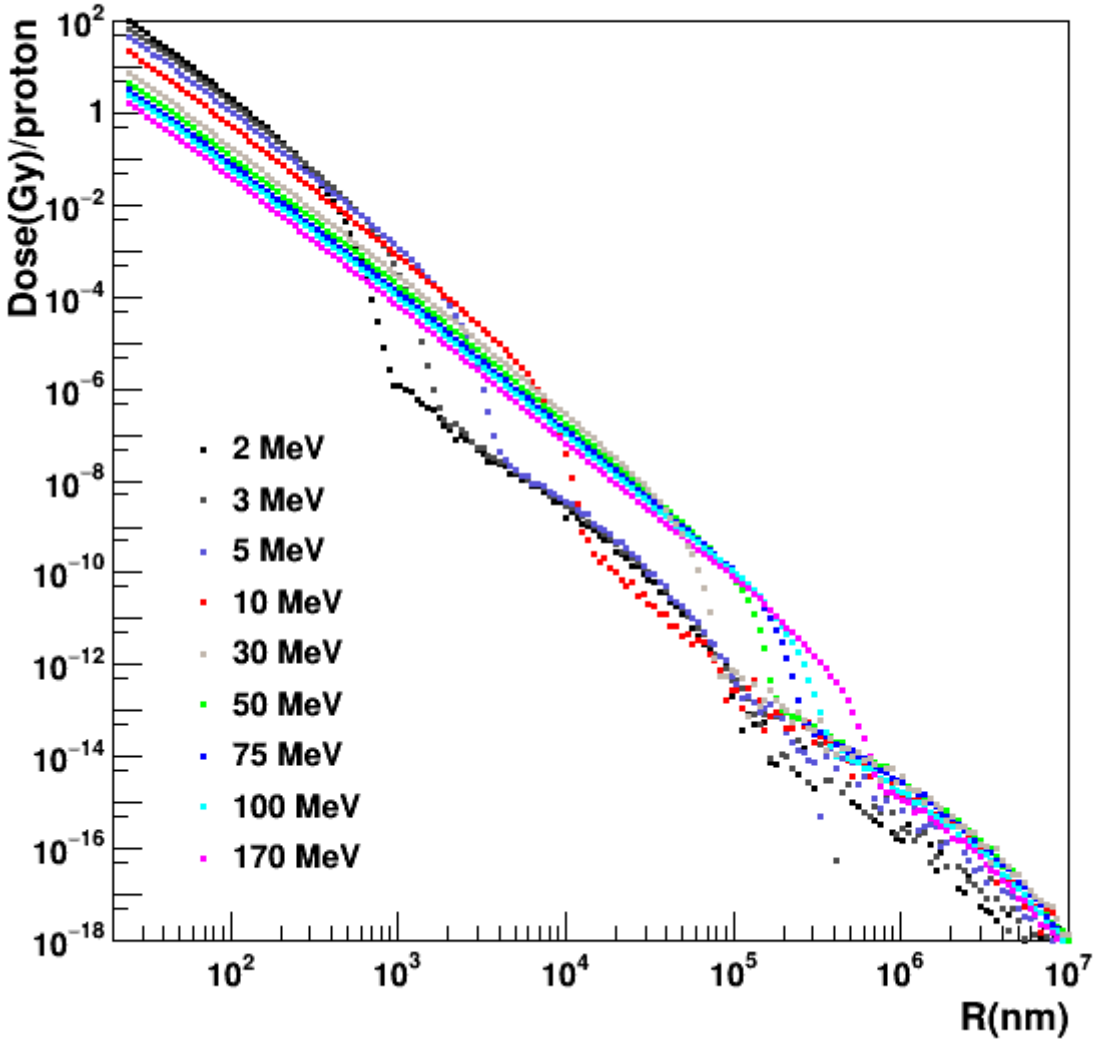

Figure 7: Absorbed radial dose distribution for GNP for 2, 3, 5, 10, 30, 50, 75, 100 and 170 MeV protons.

The contribution of photoelectrons to the absorbed radial dose distribution is observed for incident proton energies (2 MeV-170 MeV) in Figure 7 for distances larger than that defined by the gradient-discontinuity region (see also Figure 5).

Finally, Figure 8 presents the absorbed dose enhancement factor (DEF) between GNP and WNP obtained for proton beams of 2, 3, 5, 10, 50, 75, 100 and 170 MeV as a function of radial distance from the NP. The DEF is always larger than 1, demonstrating the absorbed dose increase induced by the GNP. For higher incident energies (> 10 MeV), the DEF clearly increases with radial distance up to the micron-scale and becomes nearly constant beyond. At larger distances (millimeter-scale), we observe a fast enhancement which can reach a DEF of a few hundred for low energy values, such as 2, 3, 5 and 10 MeV.

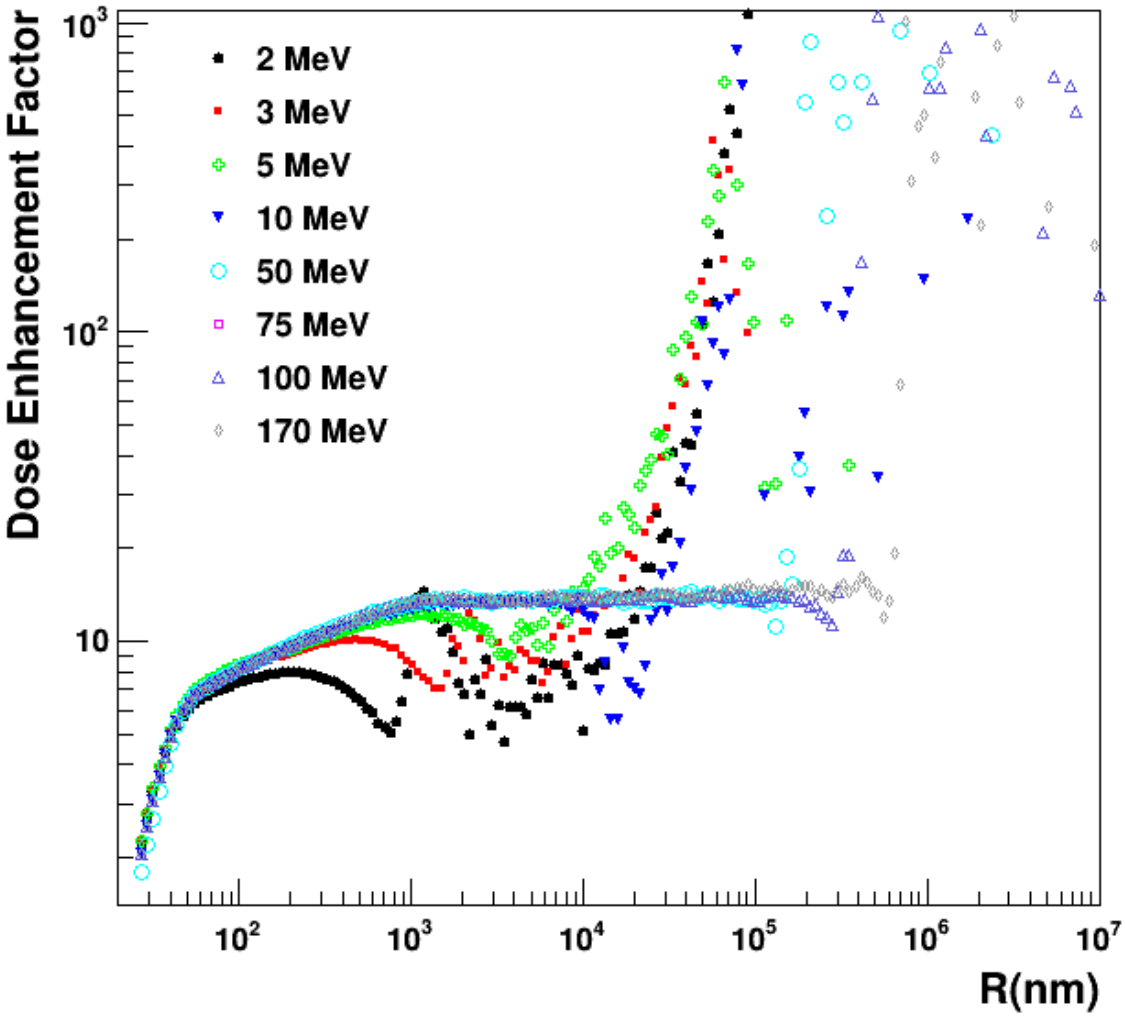

Figure 8: Absorbed Dose Enhancement Factor (DEF) obtained by mono-energetic proton of 2, 3, 5, 10, 50, 75, 100 and 170 MeV.

The behavior of the DEF for protons with incident kinetic energies of a few MeV (2, 3 and 5 MeV) for radial distances of less than 10 um from the NP is complex. These profiles, within this confined region, undergo an initial increase, followed by a decrease, and finally an increase up to large values beyond 10 um. For example, in the 2 MeV case, the DEF first increases up to 7.5 at a distance of about 200 nm, then decreases when approaching 1 µm and increases again for larger radial distances. The stages of this behavior can be explained as follows:

- For small radial distances, the DEF increases with radial distance, up to a distance (about 200 nm from the NP) corresponding to a kinetic energy equal to the mean ionization potential of gold (790 eV). This increase is due to a large number of secondary ionization electrons created in the GNP by delta electrons with kinetic energies above 790 eV and the incident proton itself. In the case of water, this limit is equal to 78 eV and the lower density of the material drastically reduces the number of generated secondary electrons. Thus, the observed increase must be considered as an approximation only as the Geant4 ionization models for incident protons (the G4BraggModel and the G4BetheBlochModel) have a low energy applicability limit equal to the mean ionization potential of the medium and they can not generate delta electrons below these values (note that this is not the case for Livermore models which are usable for electrons down to a few 10 eVs). In order to further investigate this DEF increase at small radial distances, we plan in the near future to include discrete inelastic models applicable to gold and other materials into Geant4-DNA.
- At larger radial distances, the DEF decreases. This decrease corresponds to the fall-off observed in Figure 2 and Figure 5 in the GNP and WNP: at a given incident proton energy, most energetic electrons generated by the GNP and the WNP behave similarly.

Their ranges are similar and absorbed doses for both the GNP and the WNP decrease rapidly at the end of their range. Figure 8 shows that the DEF decreases near the transition region defined by these ranges.

- Finally, beyond the range of most energetic secondary electrons (the fall-off), photoelectron interactions dominate at very large distances. Due to the larger number of secondary electrons generated by the GNP than by the WNP, more photoelectrons are generated by the GNP than by the WNP and this leads to the observed large increase of the DEF. It should be noted that high Z targets preferentially decay by fluorescence emission after inner shell ionizations (K, L, M shells), unlike low Z targets that decay mainly through Auger emission. A high-energy fluorescence X-ray produced in gold may remove electrons in water by Compton scattering or photo-electric effect. In addition, an enhancement of Bremsstrahlung production can be observed (see Figure 6) for gold when compared to that of water. These two facts lead to an increase of the secondary photon production and thus of the secondary electrons in water out of the GNP. Note that the peak between 1 and 2 µm in Figure 8 is caused by the transition between secondary electrons and photoelectrons. The observed decrease in DEF just after the peak can be attributed to the fluorescence K line photons of Oxygen in the WNP. Thus, the large increase of the DEF beyond 10 µm comes from the absence of high energy fluorescence photons generated by the WNP compared to the GNP case.

3.2. Radiolysis enhancement

Thanks to the recent addition of the modeling capabilities of physico-chemical and chemical processes in Geant4-DNA [23], it is now possible to simulate the production of radiolytic species during the so-called “physico-chemical” and “chemical” stages of water radiolysis, up to 1 µs after irradiation. After the so-called “physical” stage, excited and ionized water molecules may dissociate into new chemical species (such as e^-_{aq}, H_2, H•, •OH, H_3O^+), which can diffuse and interact mutually producing other species (such as OH^-, H_2O_2). The

dissociation scheme of excited and ionized water molecules, diffusion coefficients of diffusing species, and list of chemical reactions and reaction rates are all taken from our previous publication[30]. We performed the simulation of chemical stage up to 1 µs in order to investigate the effect of the GNP on the production of chemical species, as a function of radial dose from the GNP, time and incident proton energy. For consistency, the chemical species were scored using the same spherical shell approach employed in Section 3.1 (see Section 2.2 for more details).

- *Time-dependence of chemical species production*

Figure 9 and Figure 10 show the time evolution of the distribution of all chemical species produced by 2 MeV and 50 MeV incident protons respectively, as a function of radial distance, from either the GNP or the WNP. Results are shown at six different times after irradiation: 10 ps, 100 ps, 1 ns, 10 ns, 100 ns and 1 µs. At very short times (10 ps, 100 ps and 1 ns), radial distributions on the total number of chemical species are very similar, with the same order of magnitude, and do not show any significant time dependence. From 10 ns to 1 µs, radial distributions decrease faster with time in the closest vicinity of the NP. Indeed, in this dense area, the radiolytic species recombine to water molecules.

Figure 11 and Figure 12 show the Radiolysis Enhancement Factor (REF) for 2 MeV protons and 50 MeV protons respectively, calculated in a given shell, as the ratio of the number of chemical species generated in the presence of the GNP, to the number of chemical species generated in the presence of the WNP. At 10 ps, 100 ps and 1 ns, REFs increase and have the same dependence on radial distance. For the 2 MeV case, the enhancement increases up to 7.5 at a distance of about 200 nm, then decreases until 1000 nm. For the 50 MeV case, REFs are larger than 10 beyond 1 µm away from the NP, illustrating again the strong influence of the GNP on the production of radiolytic species compared to the water case. For both cases, from 10 ns to 1 µs, REFs increase slower as a function of time from the surface of the NP.

The observed distributions and the time independence of the REF in Figures 11 and 12 during the first few ns of the chemical phase are not unexpected.

These observed trends are due to the combination of three factors; 1) the increase in the production of chemical species is full driven by the physical stage and, as such, more species are generated in the case of the GNP than the WNP, 2) at short time scales, most of the recombination will only happen around the deposited energy points where chemical kinetics are not yet dependent on the structure of the secondary electrons , and 3) at times greater than a few ns, the radiolytic species start to diffuse away from the deposited energy positions and then become dependent on the dynamics of the track structures. The time evolution of the chemical stage is experimentally investigated through the evolution of radiochemical yields defined as the ratio of the number of a given radiolytic species to the deposited energy. The time evolution of this ratio may depend on the incident radiation LET (see for eg. [23]), underlining the strong influence of the physical stage on yields.

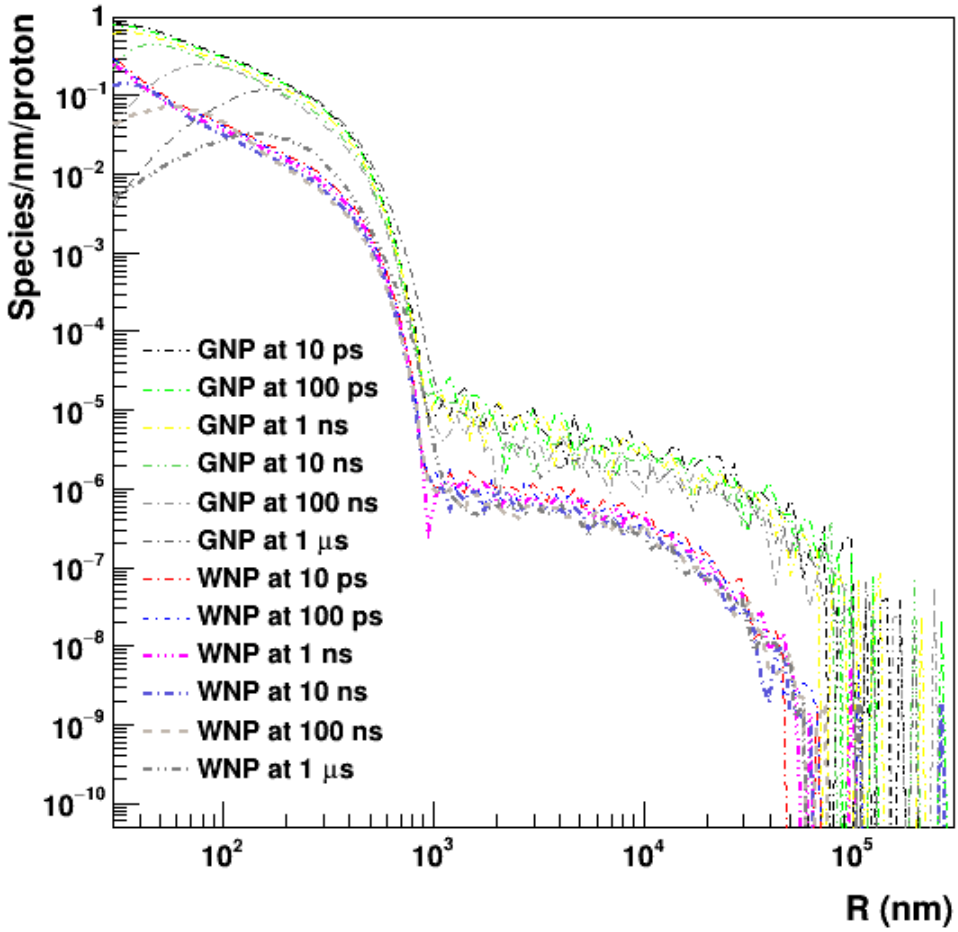

381

382 *Figure 9: Time evolution of the distribution of all radiolytic species produced by incident 2*
383 *MeV protons as a function of radial distance, either for the GNP or WNP. Results are shown at*
384 *six different times after irradiation (10 ps, 100 ps, 1 ns, 10 ns, 100 ns and 1 μs).*

385
386

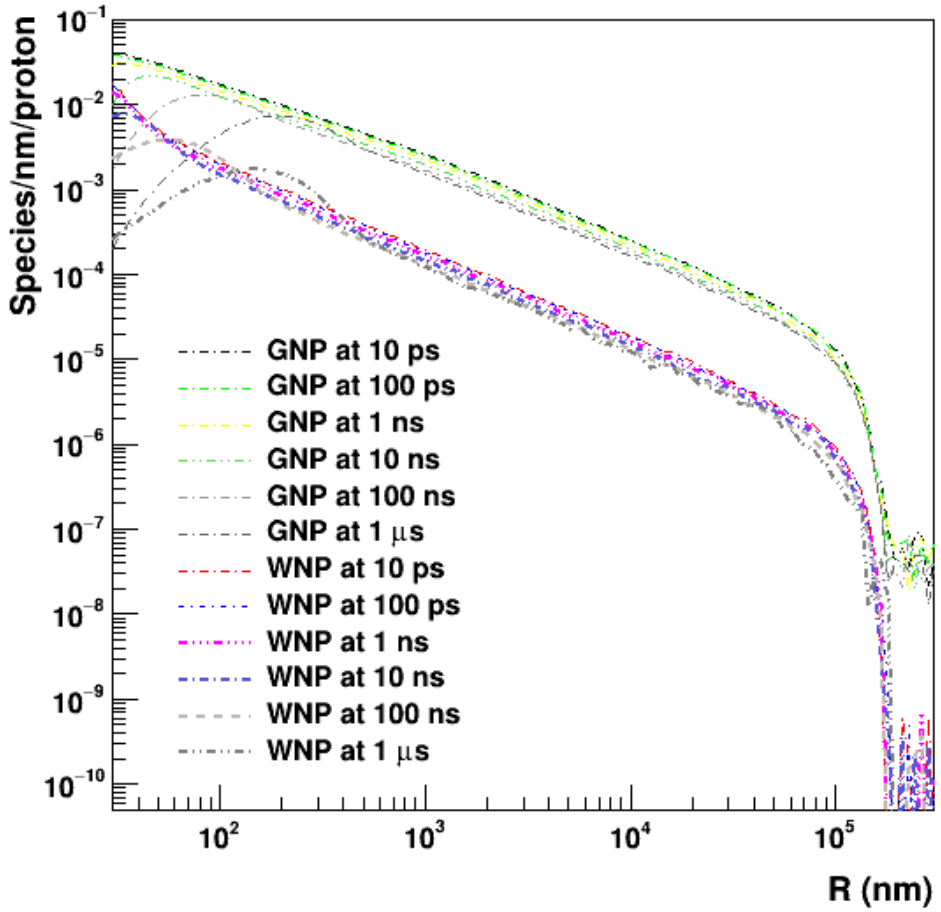

387

388 *Figure 10: Time evolution of the distribution of all chemical species produced by incident 50*
389 *MeV protons as a function of radial distance, either for the GNP or WNP. Results are shown at*
390 *six different times after irradiation (10 ps, 100 ps, 1 ns, 10 ns, 100 ns and 1 μs).*

391
392

393

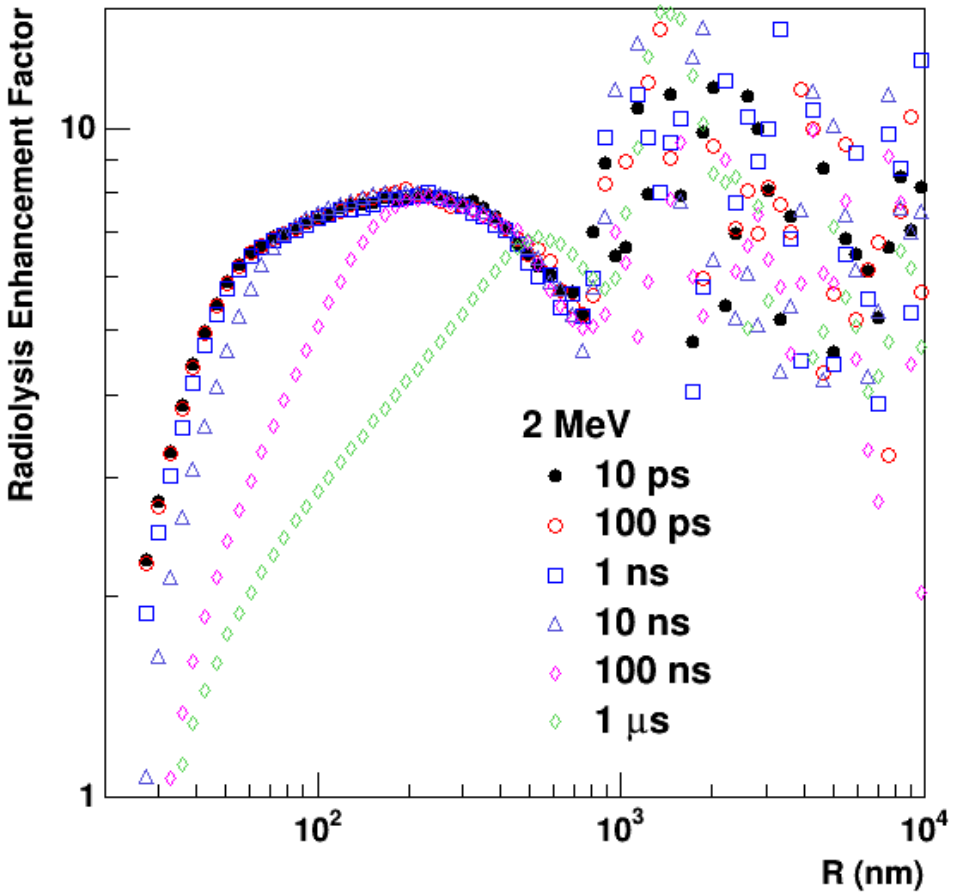

394

395 *Figure 11: Radial Radiolysis Enhancement Factor (REF) for 2 MeV protons for six time*

396 *intervals after irradiation (10 ps, 100 ps, 1 ns, 10 ns, 100 ns and 1 us)*

397

398

399

400

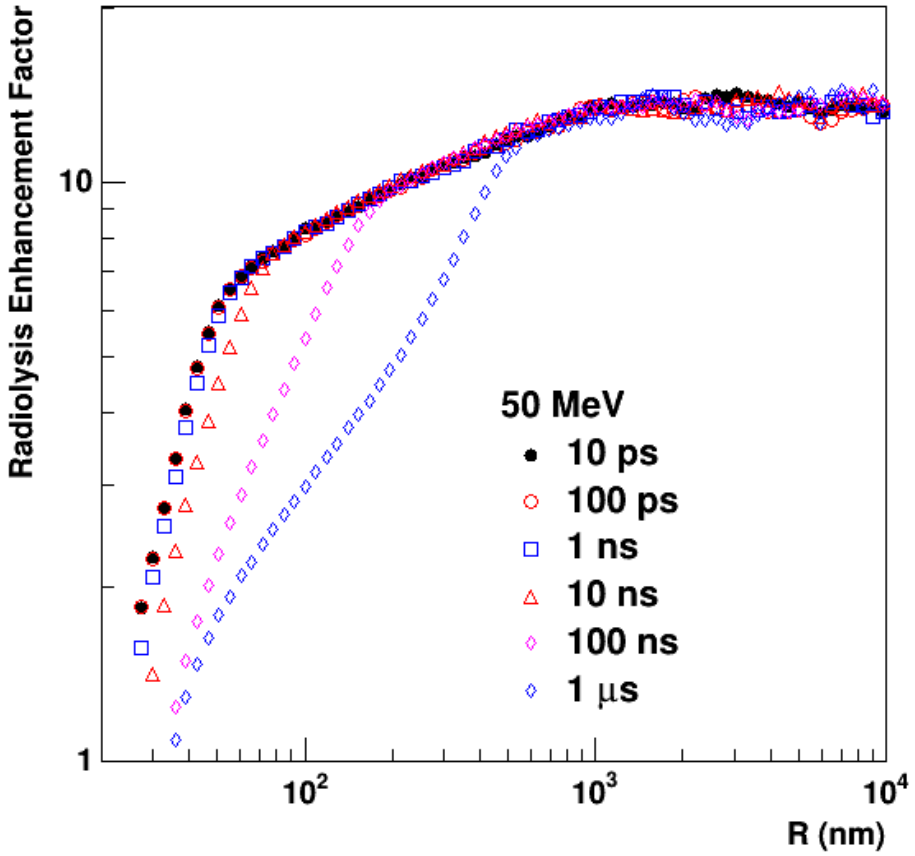

401

402 *Figure 12: Radial Radiolysis Enhancement Factor (REF) for 50 MeV protons for six time*
403 *intervals after irradiation (10 ps, 100 ps, 1 ns, 10 ns, 100 ns and 1 us).*

404 - *Incident energy dependence of radiolytic species production*

405 The energy dependence on the production of chemical species at 10 ps after irradiation is
406 presented in Figure 13 and Figure *14*. The distribution of species as a function of radial dose is
407 presented for six incident proton energies: 2, 5, 10, 50, 100 and 170 MeV. For these six
408 energies, species generated around the GNP are always in larger number than for the WNP
409 case. This is related to the larger absorbed dose observed around the GNP compared to the
410 WNP, as we previously discussed in Section 3.1. Further inspection of Figures 13 and 14 also
411 shows that there is an inverse relationship between the radial distribution of radiolytic species
412 and incident proton energy. This can be attributed to the radial absorbed dose dependence with
413 LET on the incident proton energy (discussed in Section 3.1). Further evidence of this

relationship between radiolytic species production and incident proton energy around the GNP can be seen in Figure 15. This figure presents the REF radial profiles for each of the six tested incident proton energies (2, 5, 10, 50, 100 and 170 MeV) at 10 ps after irradiation. It can be seen that the maximum REF in each radial profile before the fall-off moves further out from the edge of the GNP surface with increasing proton energy. However a non-trivial relationship between the maximum achieved REF and incident proton energy is also present, e.g. at 2 MeV a maximum REF of 7.5 can be seen at 2 MeV but it then plateaus at around 10 for the other five investigated energies.

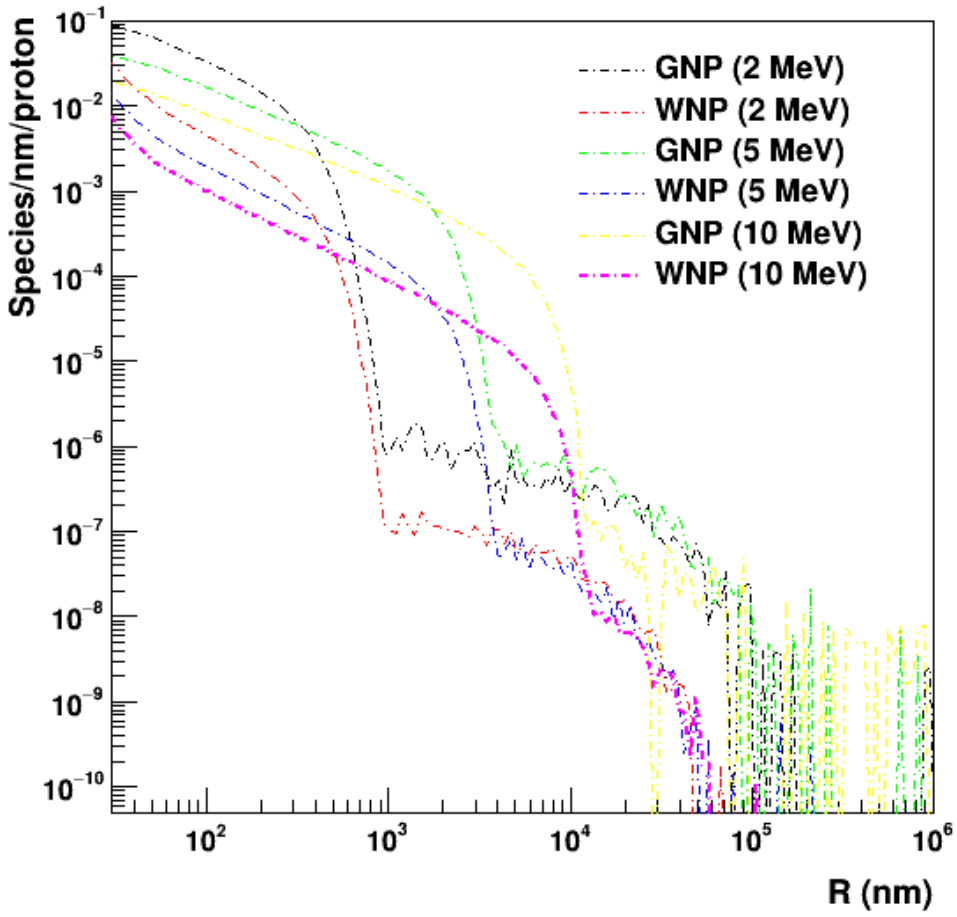

Figure 13: Distribution of radiolytic species as a function of radial distance for three incident proton energies (2, 5, 10 MeV) for the GNP and WNP, at 10 ps after irradiation.

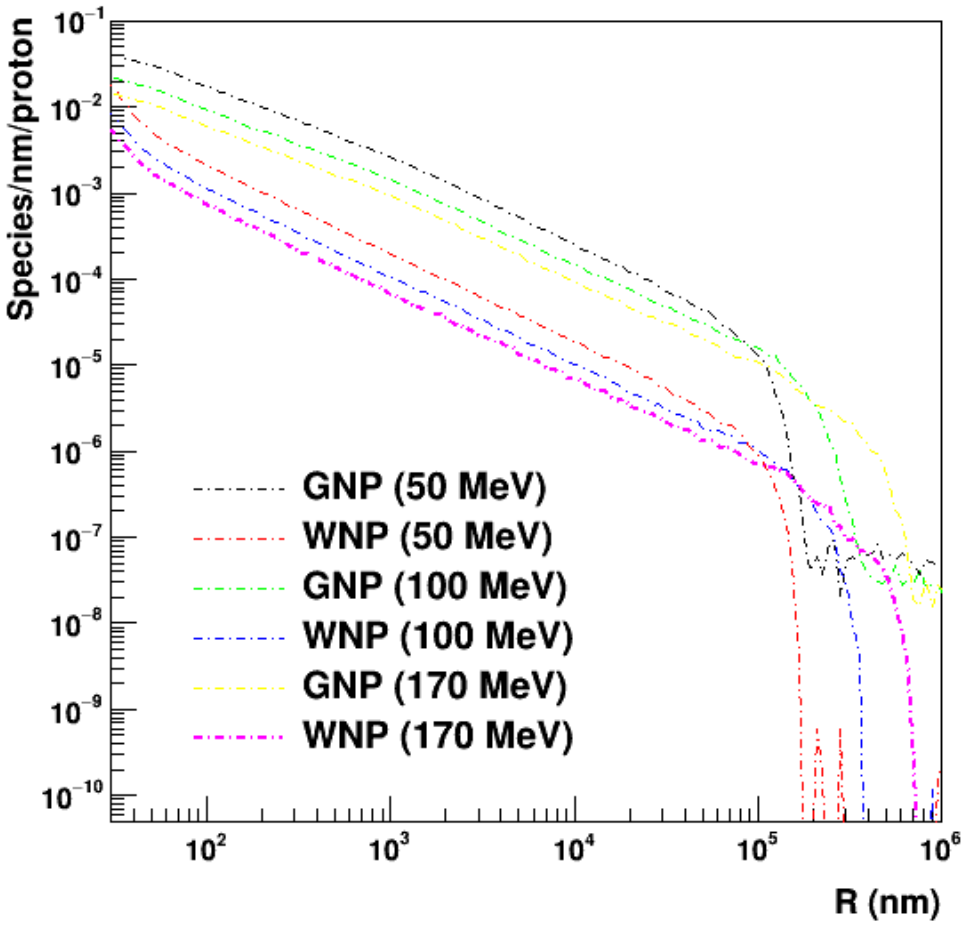

425

426 *Figure 14: Distribution of radiolytic species as a function of radial distance for three incident*

427 *proton energies (50, 100 and 170 MeV) for the GNP and WNP, at 10 ps after irradiation.*

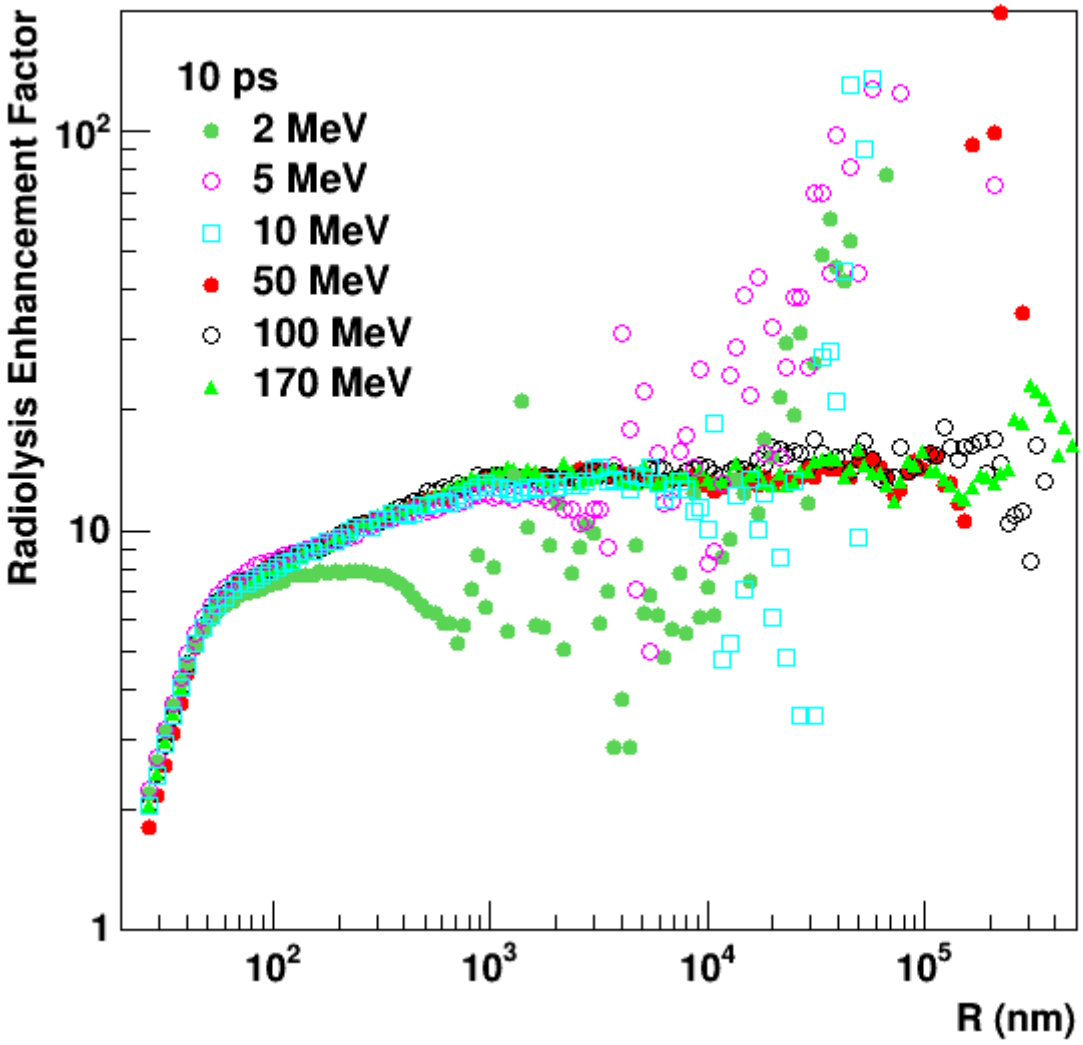

Figure 15: REF dependence with radial distance at 10 ps for six incident proton energies (2, 5, 10, 50, 100 and 170 MeV).

Figure 16 shows the distribution of radiolytic species as a function of radial distance from the surface of the GNP for all six investigated proton energies (2, 5, 10, 50, 100 and 170 MeV). For radial distances of up to about 10 um from the GNP, all distributions possess the same monotonic dependence on radius and the fall-off at larger distances. The distance at which the fall-off in REF occurs is directly proportional to incident proton energy. As the trends observed in Figure 16 match the absorbed dose profiles for the GNP shown in Figure 7, we can clearly

illustrate that the generation of chemical species is directly dependent on absorbed dose, i.e. any increase in absorbed dose outside the NP will result in an increase in chemical species production. Thus we can directly link the generated chemical species at radial distances after each profiles fall-off to the photons created during the interaction of the proton with the GNP.

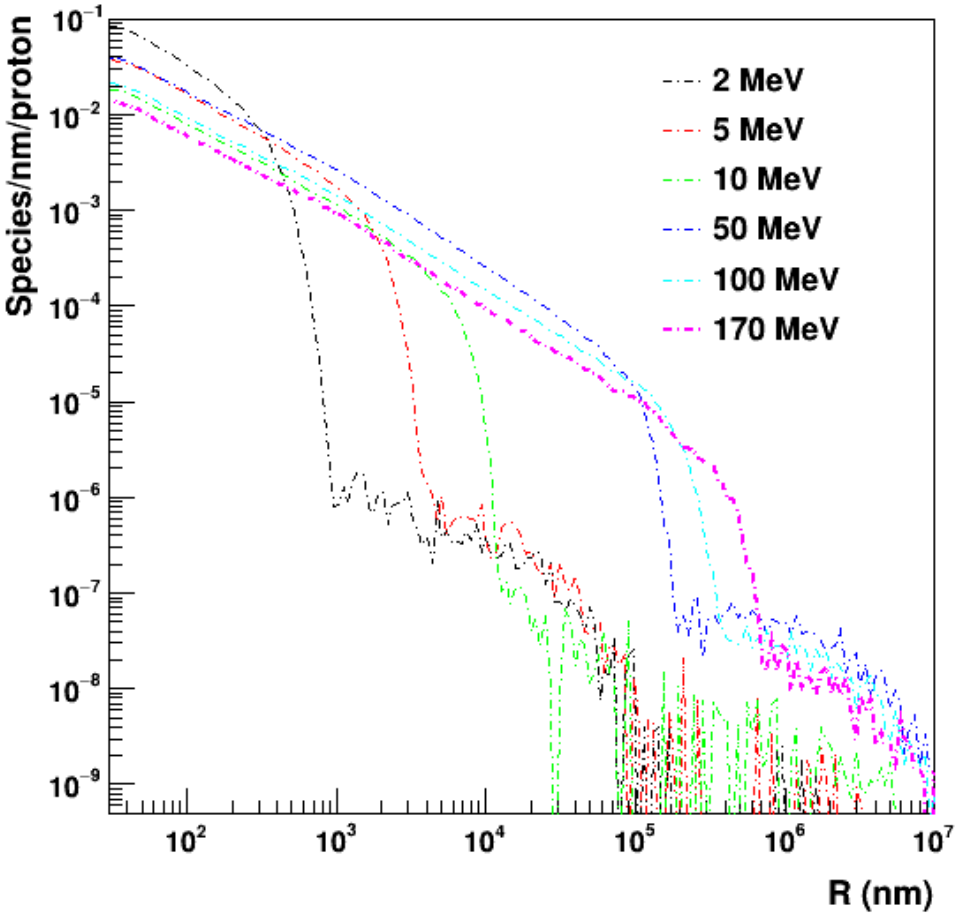

Figure 16: Radial distribution of chemical species 10 ps after irradiation for all six investigated proton energies (2, 5, 10, 50, 100 and 170 MeV) incident on the GNP.

Figure 17 shows the relative distributions of chemical species (H_3O^+, OH^-, •OH, e_{aq}^-, H•, H_2, H_2O_2) produced by incident 100 MeV protons and their time evolution from 1 ps to 1 µs, as a function of radial distance from the GNP. All distributions of chemical species have the same

dependence with radial distance. It can also be observed that the relative distributions evolve differently with time: we observe an increase for OH^-, H_2O_2 and H•, a decrease for •OH, H_3O^+ and e_{aq}^-, and a slow change for H_2. This observation is in agreement with the previously published time-dependent radiolytic yields in [23].

At short times after irradiation (1, 10, 100 ps and 1 ns), the distributions of radiolytic species from the NP are similar with the absorbed dose distribution. But from 10 ns to 1 µs, the deviation of the radiolytic species distribution compared to the absorbed dose distribution can be observed more easily as the peak of radiolytic species distribution moves in time from the close vicinity of the NP to about 200 nm (Figure 17). It should be recalled, in this case, that the incident protons were stopped when they exit the NP.

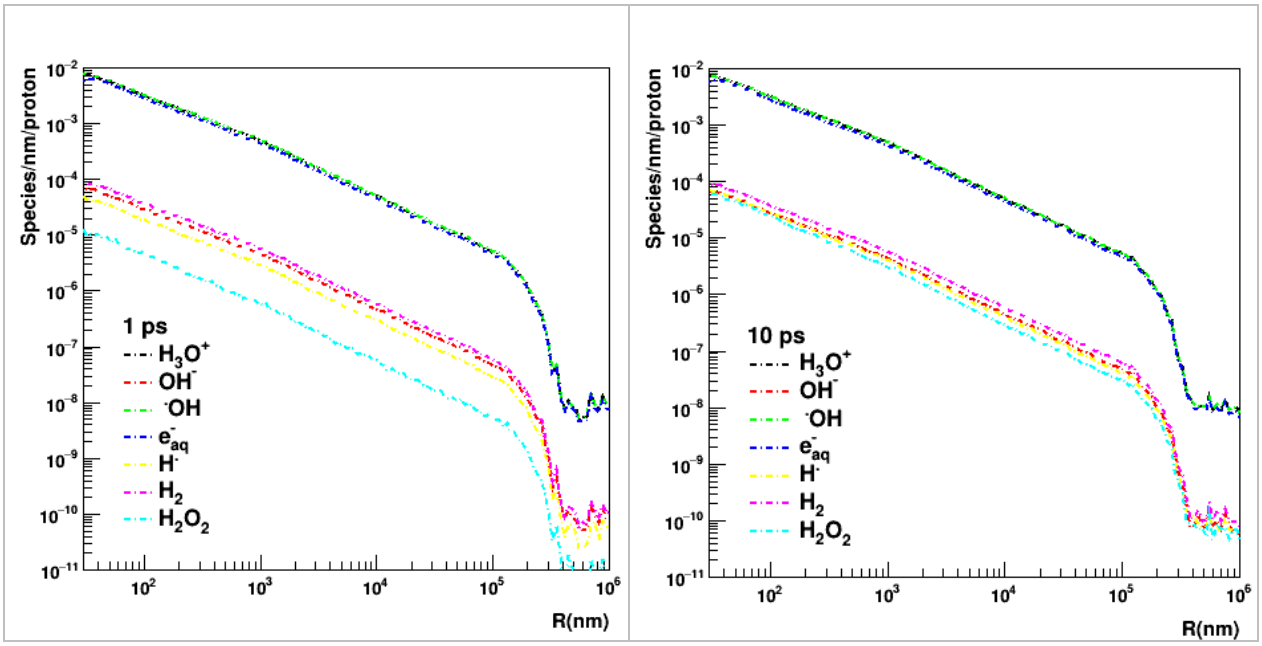

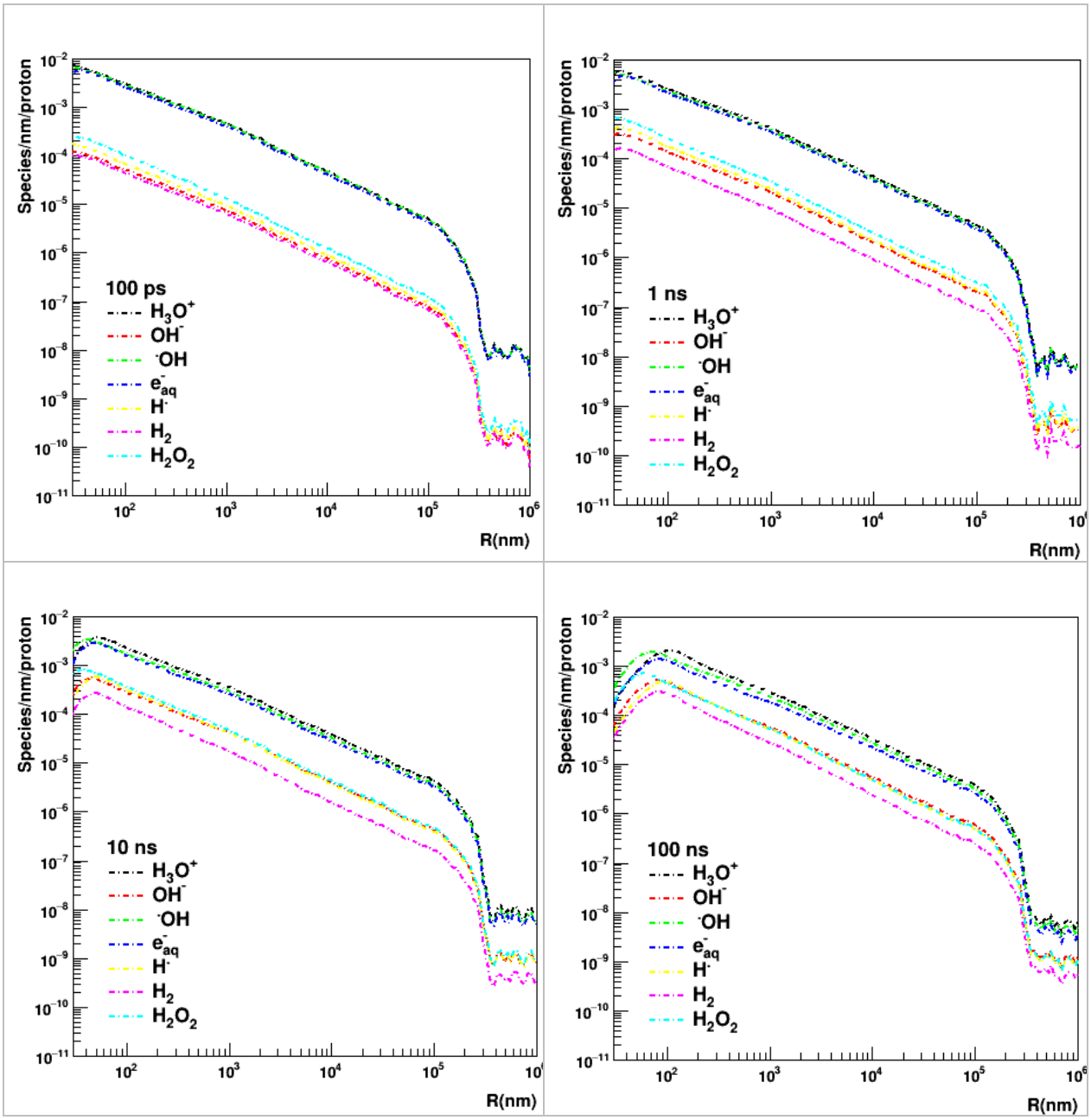
Species/nm/proton
R(nm)
100 ps
1 ns
10 ns
100 ns
H_3O^+
OH^-
$^{\cdot}OH$
e^-_{aq}
$H^{\cdot}$
H_2
H_2O_2

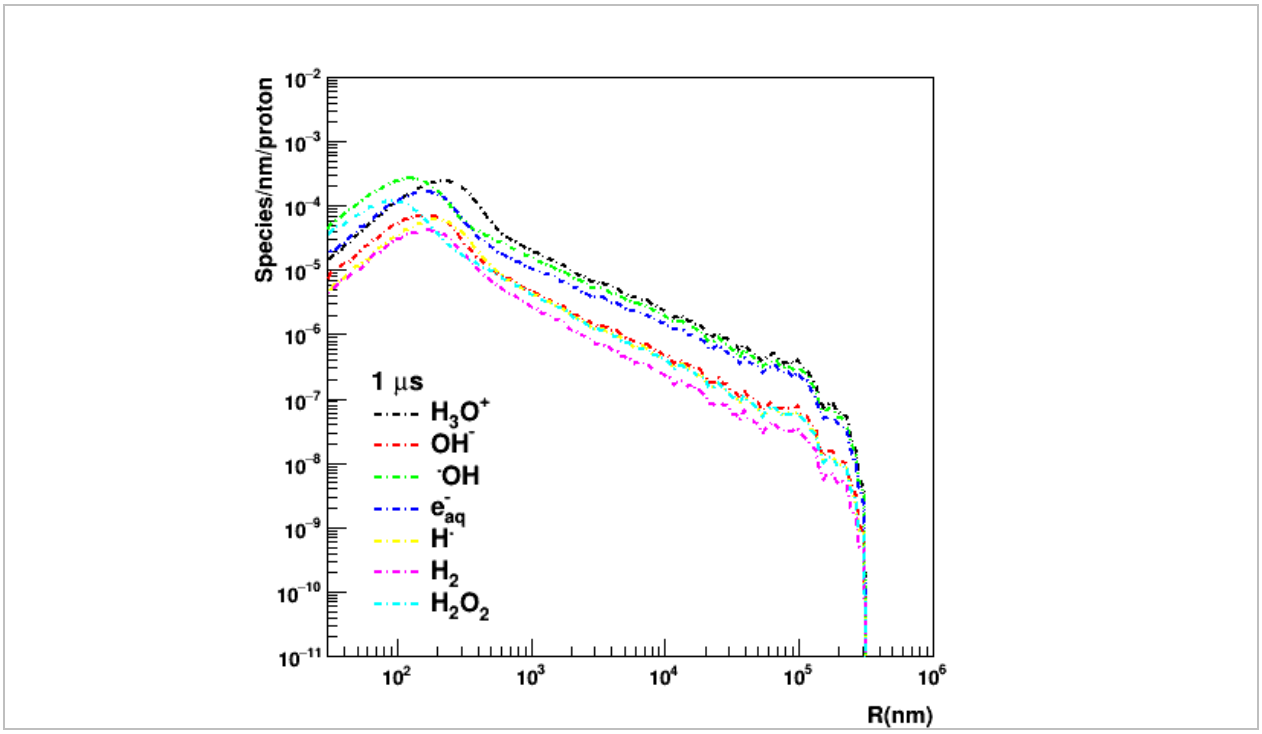

Figure 17: Time evolution of the distribution of chemical species (H_3O^+, OH^-, •OH, e_{aq}^-, H•, H_2, H_2O_2) produced by incident 100 MeV protons as a function of radial distance from the GNP. Results are shown at seven different times after irradiation (1 ps, 10 ps, 100 ps, 1 ns, 10 ns, 100 ns, 1 µs).

Figure 18 and Figure 19 show the REF of the distribution of chemical species (e_{aq}^-, •OH) produced by incident 2 MeV and 100 MeV protons as a function of radial distance from the GNP. Results at six different times after irradiation (10 ps, 100 ps, 1 ns, 10 ns, 100 ns, 1 µs) show a similar distribution for the two species.

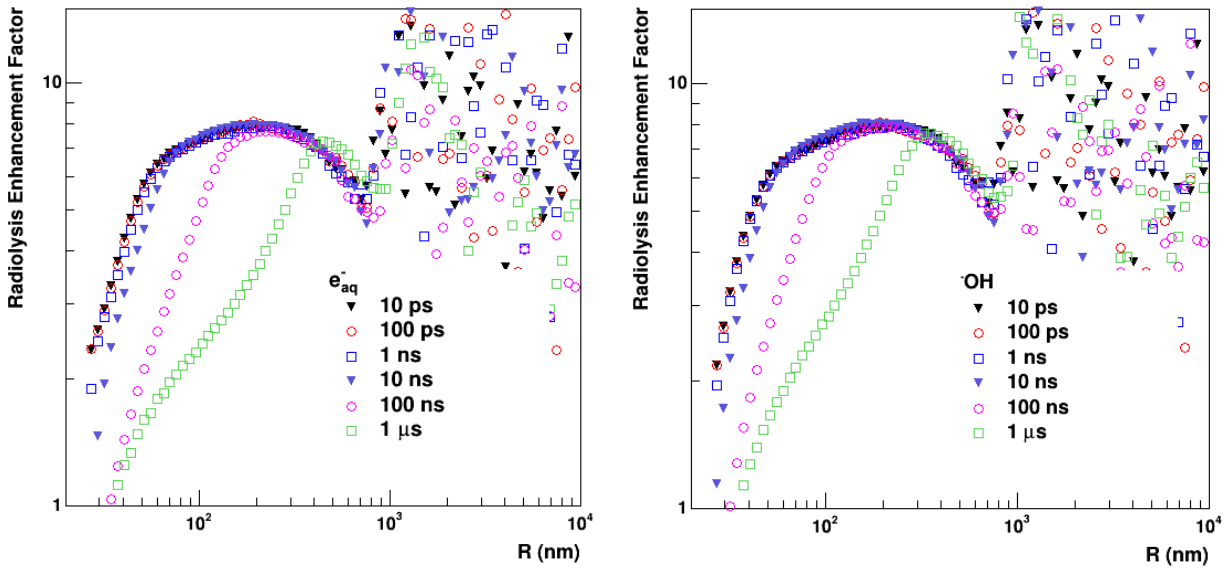

471 *Figure 18: Radiolysis Enhancement Factor (REF) of the distribution of chemical species (e_{aq}^-,*

472 *•OH) produced by incident 2 MeV protons as a function of radial distance from the NP. Results*

473 *are shown at six different times after irradiation (10 ps, 100 ps, 1 ns, 10 ns, 100 ns, 1 μs).*

474

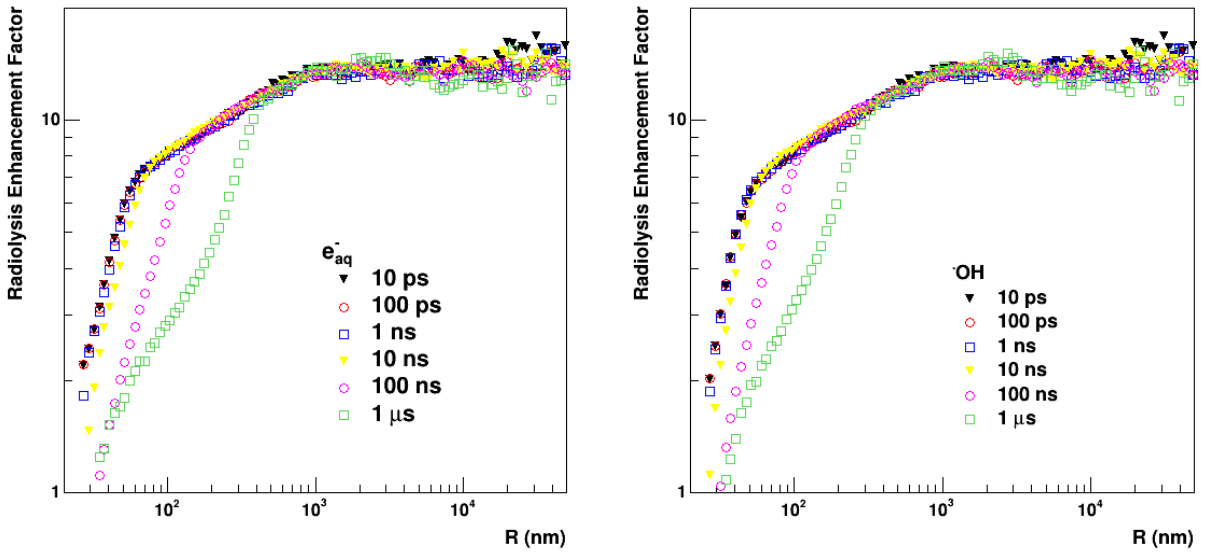

475 *Figure 19: Radiolysis Enhancement Factor (REF) of the distribution of chemical species (e_{aq}^-,*

476 *•OH) produced by incident 100 MeV protons as a function of radial distance from the NP.*

Results are shown at six different times after irradiation (10 ps, 100 ps, 1 ns, 10 ns, 100 ns, 1 µs).

The average total number of each chemical species per incident proton as a function of both evolution time and incident proton energy is presented in Table 2. Inspection of this data enables us to draw three main conclusions:

- For a given incident energy, there is a decrease with increasing time of the average number of chemical species, both for the GNP and WNP cases. This is due to the recombination of the species to liquid water.
- For a given time, there is a decrease with increasing incident energy of the average number of chemical species, both for the GNP and WNP cases. This is related to the decrease of the incident particle LET in the NP with its incident kinetic energy, in the studied energy range.
- For a given (time, energy) combination, the average number of chemical species generated around the GNP is always significantly larger than the average number of chemical species generated around the WNP. This is a direct consequence of the larger generation of secondary electrons in gold than in liquid water.

	2 MeV		5 MeV		10 MeV		50 MeV		100 MeV		170 MeV	
Time	GNP	WNP	GNP	WNP	GNP	WNP	GNP	WNP	GNP	WNP	GNP	WNP
10 ps	80.3179	14.0348	69.9185	8.5858	49.4015	5.47051	18.0477	1.71277	11.3257	0.99165	7.92319	0.693841
100 ps	75.7778	13.2372	66.1415	8.14597	47.0519	5.20458	17.2413	1.63309	10.6674	0.965804	7.62902	0.671854
1 ns	64.7229	11.4046	58.1127	7.08668	41.7588	4.5966	15.4223	1.44684	9.66332	0.861639	6.77494	0.588084
10 ns	51.979	9.2844	48.5478	5.87829	35.576	3.78756	13.3285	1.23121	8.42813	0.736346	5.76033	0.489763
100 ns	39.0212	8.16022	39.3362	5.14844	29.541	3.33195	11.632	1.0945	7.35567	0.660627	4.94079	0.424286
1 µs	31.9774	7.68632	33.4445	4.75699	25.8717	3.11938	10.4302	1.01443	6.58677	0.635982	4.3565	0.405011

Table 2: Average numbers of radiolytic species generated per incident proton around the GNP and WNP at different times after the physical stage.

4. Conclusion

For the first time, we have presented in this work the combination of Geant4 physics modeling capabilities with Geant4-DNA physics, physico-chemical and chemical modeling capabilities, for the study of the irradiation of a gold spherical nanoparticle immersed in liquid water by an incident proton beam. This combination allowed us studying the absorbed dose enhancement and the production of chemical species around the nanoparticle for different incident energies (2 MeV – 170 MeV) and at different times after irradiation up to 1 µs. The reader should however keep in mind that the physico-chemical and chemical module of Geant4-DNA is still in a prototype state. The presented results may be affected by the evolution of the description of the processes, in particular in the physico-chemical stage, as for instance the electron-cation recombination or the way the radiolytic products are placed after water dissociation, which is a source of uncertainty for this type of modeling. Moreover, Geant4 existing ionization models for incident protons (the G4BraggModel and the G4BetheBlochModel) cannot simulate the production of delta electrons below the mean ionization potential of the medium, leading to an underestimation of the number of delta electrons at very low energies. This may directly influence the DEF in close vicinity of the NP as well as the associated production of chemical species.

The simulation of Dose Enhancement Factors (DEF) and Radiolysis Enhancement Factors (REF) between GNP and WNP as a function of radial distance show similar trends for the simulated incident proton energy range. While lower incident proton energies show higher absorbed dose distribution near the NP, higher DEF and REF are found with higher incident proton energies: there is thus a competition near the NP between DEF (and REF) on one side, and absorbed dose distribution on the other side, as a function of incident proton energy. Further mechanistic investigation at larger scale (for example at the cellular or tissue scale), taking into account the full transport of protons in the water medium, and using a larger

number of NPs (including a study of coating influence) is still required before being able to draw any conclusion related to possible benefits of using gold NPs in proton irradiation. However, this work illustrates the current technical capabilities of the Geant4-DNA extension for further study of involved physical, physico-chemical and chemical mechanisms.

Acknowledgements

We would like to acknowledge Ton Duc Thang University for giving us access to the University computing facilities. Finally, we deeply thank the Computing Research Center, KEK, Tsukuba, Japan, for offering us computing resources for the simulations presented in this work. This research is funded by Vietnam National Foundation for Science and Technology Development (NAFOSTED) under grant number ”10001920101”.

534

535 **References**

536 [1] H. Matsudaira H, A. M. Ueno and I. Furuno, Iodine contrast medium sensitizes cultured
537 mammalian cells to x-rays but not to γ rays, Radiat. Res. 84 (1980) 144–8

538 [2] W. Hadnagy, A. Bauml and G. Stephan, Energy-dependent effect of iodized contrast
539 medium on radiation-induced chromosome aberrations, Radiat Environ Biophys 24
540 (1985) 71-74

541 [3] R. S. Mello, H. Callison, J. Winter, A. R. Kagan and A. Norman A, Radiation dose
542 enhancement in tumours with iodine Med. Phys. 10 (1983) 75–8

543 [4] P. Dawson, M. Penhaligon, E. Smith and J. Saunders, Iodinated contrast agents as
544 'radiosensitizers', British Journal of Radiology 60 (1987) 201–203

545 [5] N. Tokita, Y. Akime, S. Egawa and M. R. Raju, Biological dosimetry for iodine contrast
546 medium and X-ray interactions by cell survival, British Journal of Radiology 63
547 (1990) 735–737

548 [6] K. S. Iwamoto, S. T. Cochran, J. Winter, E. Holburt, R. T. Higashida and A. Norman,
549 Radiation dose enhancement therapy with iodine in rabbit VX-2 brain tumors,
550 Radiotherapy and Oncology 8 (1987) 161-170

551 [7] N. Lewinski, V. Colvin, and R. Drezek, Cytotoxicity of Nanoparticles, Small 4 (2008) 1, 26
552 – 49

553 [8] E. E. Connor, J. Mwamuka, A. Gole, C. J. Murphy and M. D. Wyatt, Gold Nanoparticles
554 Are Taken Up by Human Cells but Do Not Cause Acute Cytotoxicity, Small 1
555 (2005) 3, 325 –327

556 [9] D. F. Regulla, L. B. Hieber and M. Seidenbusch, Physical and biological interface dose
557 effects in tissue due to x-ray-induced release of secondary radiation from metallic

gold surfaces, Radiat. Res. 150 (1998) 92–100

[10] D. M. Herold, I. J. Das, C. C. Stobbe, R. V. Iyer and J. D. Chapman, Gold microspheres: a selective technique for producing biologically effective dose enhancement, Int. J. Radiat. Biol. 76 (2000) 1357–64

[11] J. F. Hainfeld, D. N. Slatkin and H. M. Smilowitz, The use of gold nanoparticles to enhance radiotheraphy in mice, Phys. Med. Biol. 49 (2004) N309-N315

[12] D. B. Chithrani,S. Jelveh, F. Jalali, M. V. Prooijen, C. Allen. R. G. Bristow, R. P. Hill and D. A. Jaffray, Gold Nanoparticles as Radiation Sensitizers in Cancer Therapy, Radiat. Res. 173 (2010) 719–728

[13] C. J. Liu, C. H. Wang, S. T. Chen, H. H. Chen, W. H. Leng, C. C. Chien, C. L. Wang, I. M. Kempson, Y. Hwu, T. C. Lai, M. Hsiao, C. S. Yang, Y. J. Chen and G. Margaritondo, Enhancement of cell radiation sensitivity by pegylated gold nanoparticles, Phys. Med. Biol. 55 (2010) 931–945

[14] J. K. Kim, S. J. Seo, H. T. Kim, K. H. Kim, M. H. Chung, K. R. Kim and S. J. Ye, Enhanced proton treatment in mouse tumors through proton irradiated nanoradiator effects on metallic nanoparticles, Phys. Med. Biol. 57 (2012) 8309–8323

[15] I. El Naqa, P. Pater and J. Seuntjens, Monte Carlo role in radiobiological modelling of radiotherapy outcomes, Phys. Med. Biol. 57 (2012) R75–R97

[16] E. Lechtman, S. Mashouf, N. Chattopadhyay, B. M. Keller, P. Lai, Z. Cai, R. M. Reilly and J-P. Pignol, A Monte Carlo-based model of gold nanoparticle radiosensitization accounting for increased radiobiological effectiveness, Phys. Med. Biol. 58 (2013) 3075–3087

[17] S. J. McMahon, W. B. Hyland, M. F. Muir, J. A. Coulter, S. Jain, K. T. Butterworth, G. Schettino, G. R. Dickson, A. R. Hounsell, J. M. O'Sullivan, K. M. Prise, D. G. Hirst

582 and F. J. Currell, Biological consequences of nanoscale energy deposition near
583 irradiated heavy atom nanoparticles, SCIENTIFIC REPORTS (2011) 1-18

584 [18] S. J. McMahon, W. B. Hyland, M. F. Muir, J. A. Coulter, S. Jain, K. T. Butterworth, G.
585 Schettino, G. R. Dickson, A. R. Hounsell, J. M. O'Sullivan, K. M. Prise, D. G. Hirst,
586 F. J. Currell, Nanodosimetric effects of gold nanoparticles in megavoltage radiation
587 therapy, Radiotherapy and Oncology, 100 (2011) 412–416

588 [19] S. H. Cho, Estimation of tumour dose enhancement due to gold nanoparticles during
589 typical radiation treatments: a preliminary Monte Carlo study, Phys. Med. Biol. 50
590 (2005) N163–N173

591 [20] B. L. Jones, S. Krishnan and S. H. Cho, Estimation of microscopic dose enhancement
592 factor around gold nanoparticles by Monte Carlo calculations Med. Phys. 37 (2010)
593 3809–16

594 [21] Y. Lin, S. J. McMahon, M. Scarpelli, H. Paganetti and J. Schuemann, Comparing gold
595 nano-particle enhanced radiotherapy with protons, megavoltage photons and
596 kilovoltage photons: a Monte Carlo simulation, Phys. Med. Biol. 59 (2014) 7675–
597 7689

598 [22] S. Baluchamy, P. Ravichandran, A. Periyakaruppan, V. Ramesh, J. C. Hall, Y. Zhang, O.
599 Jejelowo, D. S. Gridley, H. Wu and G. T. Ramesh, Induction of cell death through
600 alteration of oxidants and antioxidants in lung epithelial cells exposed to high energy
601 protons J. Biol. Chem. 285 (2010) 24769–74

602 [23] M. Karamitros, S. Luan, M. A. Bernal, J. Allison, G. Baldacchino, M. Davidkova,
603 Z.Francis, W. Friedland, V. Ivantchenko, A. Ivantchenko, A. Mantero, P. Nieminem,
604 G. Santin, H. N. Tran, V. Stepan and S.Incerti, Diffusion-controlled reactions
605 modelingin Geant4-DNA, Journal of Computational Physics 274 (2014) 841–882

606 [24] S. Incerti, A. Ivanchenko, M. Karamitros, A. Mantero, P. Moretto, H.N.Tran, B.
607 Mascialion, C. Champion, V. N. Ivanchenko, M. A. Bernal, Z. Francis, C. Villagrasa,
608 G. Baldacchino, P. Gueye, R. Capra, P. Nieminen, C. Zacharatou, Comparion of
609 GEANT4 very low energy cross section models with experimental data in water,
610 Med. Phys. 37 (2010) 4692-4708

611 [25] S. Agostinelli, J. Allison, K. Amako, J. Apostolakis, H. Araujo, P. Arce, M. Asai, D.
612 Axen, S. Banerjee, G. Barrand, F. Behner, L. Bellagamba, J. Boudreau, L. Broglia, A.
613 Brunengo, H. Burkhardt, S. Chauvie, J. Chuma, R. Chytracek, G. Cooperman, G.
614 Cosmo, P. Degtyarenko, A. Dell'Acqua, G. Depaola, D. Dietrich, R. Enami, A.
615 Feliciello, C. Ferguson, H. Fesefeldt, G. Folger, F. Foppiano, A. Forti, S. Garelli, S.
616 Giani, R. Giannitrapani, D. Gibin, J.J. Gómez Cadenas, I. González, G. Gracia Abril,
617 G. Greeniaus, W. Greiner, V. Grichine, A. Grossheim, S. Guatelli, P. Gumplinger, R.
618 Hamatsu, K. Hashimoto, H. Hasui, A. Heikkinen, A. Howard, V. Ivanchenko, A.
619 Johnson, F.W. Jones, J. Kallenbach, N. Kanaya, M. Kawabata, Y. Kawabata, M.
620 Kawaguti, S. Kelner, P. Kent, A. Kimura, T. Kodama, R. Kokoulin, M. Kossov, H.
621 Kurashige, E. Lamanna, T. Lampén, V. Lara, V. Lefebure, F. Lei, M. Liendl, W.
622 Lockman, F. Longo, S. Magni, M. Maire, E. Medernach, K. Minamimoto, P. Mora de
623 Freitas, Y. Morita, K. Murakami, M. Nagamatu, R. Nartallo, P. Nieminen, T.
624 Nishimura, K. Ohtsubo, M. Okamura, S. O'Neale, Y. Oohata, K. Paech, J. Perl, A.
625 Pfeiffer, M.G. Pia, F. Ranjard, A. Rybin, S. Sadilov, E. Di Salvo, G. Santin, T.
626 Sasaki, N. Savvas, Y. Sawada, S. Scherer, S. Sei, V. Sirotenko, D. Smith, N. Starkov,
627 H. Stoecker, J. Sulkimo, M. Takahata, S. Tanaka, E. Tcherniaev, E. Safai Tehrani, M.
628 Tropeano, P. Truscott, H. Uno, L. Urban, P. Urban, M. Verderi, A. Walkden, W.
629 Wander, H. Weber, J.P. Wellisch, T. Wenaus, D.C. Williams, D. Wright, T. Yamada,
630 H. Yoshida, D. Zschiesche, G4--a simulation toolkit, Nuclear Instruments and

631 Methods in Physics Research Section A: Accelerators, Spectrometers, Detectors and
632 Associated Equipment, 506 (2003) 250-303.

633 [26] J. Allison, K. Amako, J. Apostolakis, H. Araujo, P.A. Dubois, M. Asai, G. Barrand, R.
634 Capra, S. Chauvie, R. Chytracek, G.A.P. Cirrone, G. Cooperman, G. Cosmo, G.
635 Cuttone, G.G. Daquino, M. Donszelmann, M. Dressel, G. Folger, F. Foppiano, J.
636 Generowicz, V. Grichine, S. Guatelli, P. Gumplinger, A. Heikkinen, I. Hrivnacova,
637 A. Howard, S. Incerti, V. Ivanchenko, T. Johnson, F. Jones, T. Koi, R. Kokoulin, M.
638 Kossov, H. Kurashige, V. Lara, S. Larsson, F. Lei, O. Link, F. Longo, M. Maire, A.
639 Mantero, B. Mascialino, I. McLaren, P.M. Lorenzo, K. Minamimoto, K. Murakami,
640 P. Nieminen, L. Pandola, S. Parlati, L. Peralta, J. Perl, A. Pfeiffer, M.G. Pia, A.
641 Ribon, P. Rodrigues, G. Russo, S. Sadilov, G. Santin, T. Sasaki, D. Smith, N.
642 Starkov, S. Tanaka, E. Tcherniaev, B. Tome, A. Trindade, P. Truscott, L. Urban, M.
643 Verderi, A. Walkden, J.P. Wellisch, D.C. Williams, D. Wright, H. Yoshida, Geant4
644 developments and applications, Nuclear Science, IEEE Transactions on, 53 (2006)
645 270-278

646 [27] S. Incerti, G. Baldacchino, M. Bernal, R. Capra, C. Champion, Z. Francis, S. Guatelli, P.
647 Guèye, A. Mantero, B. Mascialino, P. Moretto, P. Nieminen, A. Rosenfeld, C.
648 Villagrasa and C. Zacharatou, The Geant4-DNA project, Int. J. Model. Simul. Sci.
649 Comput. 1 (2010) 157–178

650 [28] S. Incerti, C. Champion, H. N. Tran, M. Karamitros, M. Bernal, Z. Francis, V.
651 Ivanchenko, A. Mantero, Members of the Geant4-DNA collaboration, Energy
652 deposition in small-scale targets of liquid water using the very low energy
653 electromagnetic physics processes of the Geant4 toolkit, Nuc. Inst. and Meth. Phys.
654 Res B 306 (2013) 158-164

655 [29] H. N. Tran, Z. El Bitar, C. Champion, M. Karamitros, M.A. Bernal, Z. Francis, V.

Ivantchenko, S.B. Lee, J.I. Shin and S. Incerti, Modeling proton and alpha elastic scattering in liquid water in Geant4-DNA, Nuc. Inst. and Meth. Phys. Res B 343 (2015) 132–137

[30] M. Karamitros, A. Mantero, S. Incerti, G. Baldacchino, P. Barberet, M. Bernal, R. Capra, C. Champion, Z. El Bitar, Z. Francis, et al., Modeling radiation chemistry in the Geant4 Toolkit, Progr. Nucl. Sci. Technol. 2 (2011) 503–508

[31] Physics Reference Manual, Version: geant4 10.1 (5 December 2014)

[32] A. Thompson, D. Attwood, E. Gullikson, M. Howells, K.-J. Kim, J. Kirz, J. Kortright, I. Lindau, Y. Liu, P. Pianetta, A. Robinson, J. Scofield, J. Underwood, G. Williams, X-Ray Data booklet, (2009).